UNIVERSIDAD DE CONCEPCIÓN

Centro de Investigación en Ingeniería Matemática (CI^{2}MA)

Mixed Kirchhoff stress - displacement - pressure formulations for incompressible hyperelasticity

Patrick E. Farrell, Luis F. Gatica,
Bishnu Lamichhane, Ricardo Oyarzúa,
Ricardo Ruiz-Baier

PREPRINT 2020-17

SERIE DE PRE-PUBLICACIONES

Mixed Kirchhoff stress - displacement - pressure formulations for incompressible hyperelasticity

Patrick E. Farrell[*] Luis F. Gatica[†] Bishnu Lamichhane[‡]
Ricardo Oyarzúa[§] Ricardo Ruiz-Baier[¶]

July 2, 2020

Abstract

We adapt the three-field formulation for nearly incompressible hyperelasticity introduced in [Chavan, Lamichhane, Wohlmuth, Comput. Methods Appl. Mech. Engrg. (2007), **196**:4075–4086] to the fully incompressible case. We also discuss the solvability of the linearised problem restricted to simple material laws. We construct a mixed finite element scheme for simplicial meshes and verify its error decay through computational tests. We also propose a new augmented Lagrangian preconditioner that improves convergence properties of iterative solvers. A few benchmark solutions are computed, and we test the formulation in models of cardiac biomechanics using orthotropic strain energy densities.

1 Introduction

Mixed methods for nonlinear solid mechanics consider additional fields in the variational formulation, minimising suitable energy functionals and using further constraints. Approaches based on the Hu–Washizu and Hellinger–Reissner principles are among the most popular choices, and they often lead to saddle-point problems where suitable inf-sup conditions need to be satisfied (see e.g. [12,43]). Recent variants of these methods include mixed (first Piola–Kirchhoff) stress tensor and displacement formulations, introduced in [31]. These arise from inversion of the constitutive relations. Also, a HDG method based on the minimisation of the potential energy has been analysed in [26], where the authors also discuss when the convergence is compromised and propose a stabilisation strategy. Mixed formulations involving pseudo-stress, displacement and pressure have been studied in [16]. Recent comparisons between different discontinuous approximations can be found in [7] and between least-squares mixed formulations in [38]. Recent preconditioners tailored for hyperelasticity of soft tissue can be found in [14, 42].

More relevant to the present case, formulations in terms of Kirchhoff stress, displacement and pressure were introduced in [15] and have been adapted to the study of cardiac electromechanics in [33,36]. Recasting the three-field formulation in this particular set of unknowns is very useful for modelling the physiological responses of cardiac tissue, as the Kirchhoff stress tensor acts as the coupling field with the equations describing electrical propagation. It thus allows for the direct approximation of the variables of interest [36].

[*]Mathematical Institute, University of Oxford, Andrew Wiles Building, Woodstock Road, Oxford OX2 6GG, UK. E-mail: patrick.farrell@maths.ox.ac.uk.

[†]Departamento de Matemática y Física Aplicadas, Universidad Católica de la Santísima Concepción, Casilla 297, Concepción, Chile; and Centro de Investigación en Ingeniería Matemática (CI^{2}MA), Universidad de Concepción, Chile. E-mail: lgatica@ucsc.cl.

[‡]School of Mathematical and Physical Sciences, The University of Newcastle, Callaghan, NSW 2308, Australia. Email: bishnu.lamichhane@newcastle.edu.au.

[§]GIMNAP, Departamento de Matemática, Universidad del Bío-Bío, Concepción, Chile; and Centro de Investigación en Ingeniería Matemática (CI^{2}MA), Universidad de Concepción, Chile. E-mail: royarzua@ubiobio.cl.

[¶]School of Mathematical Sciences, Monash University, 9 Rainforest Walk, 3800 VIC, Australia. E-mail: ricardo.ruizbaier@monash.edu.

An additional key feature is that the formulation imposes symmetry of the stress without the need for additional reconstruction or complicated element choices. Solving the three-field formulation using a suitable discretisation also avoids volumetric locking. However, the size of the systems involved leads to rather high computational costs, thus making the adoption of robust and efficient iterative solvers important. Within the context of cardiac mechanics, the performance of numerical solvers is particularly crucial to clinical applications. The primary difficulties not only lie with the high spatial and temporal resolutions required by the simulations of patient-specific physiological conditions, but also with the time constraints posed by clinical diagnosis. As a result, the use of preconditioning techniques is mandatory for lowering the computational cost associated with diagnostic-oriented simulations.

Let us recall that (left) preconditioning improves the spectral properties of a general linear system [41] by pre-multiplying both sides of the equation with a matrix $\mathcal{P}^{-1}$:

$$\begin{aligned} &\mathcal{A}u = b \\ \implies &\mathcal{P}^{-1}\mathcal{A}u = \mathcal{P}^{-1}b. \end{aligned} \tag{1.1}$$

Roughly speaking, the quality of a preconditioner depends on how closely $\mathcal{P}^{-1}$ can approximate the exact inverse of $\mathcal{A}$; the better the approximation, the higher the quality [11]. The choice of $\mathcal{P}^{-1}$ for block systems relies heavily on knowledge about the block structure of $\mathcal{A}$. For a general non-singular 2×2 block matrix with a non-singular top-left block A,

$$\mathcal{A} = \begin{bmatrix} A & B \\ C & D \end{bmatrix}, \tag{1.2}$$

a popular class of preconditioners builds on the block factorisation formula [10, 18, 25, 32, 41]

$$\mathcal{A}^{-1} \approx \mathcal{P}^{-1} = \begin{bmatrix} I & -\hat{A}^{-1}B \\ 0 & I \end{bmatrix} \begin{bmatrix} \hat{A}^{-1} & 0 \\ 0 & \hat{S}^{-1} \end{bmatrix} \begin{bmatrix} I & 0 \\ -C\hat{A}^{-1} & I \end{bmatrix}, \tag{1.3}$$

where $\hat{A}^{-1}$ and $\hat{S}^{-1}$ are respectively approximations of A^{-1} and S^{-1}, with $S = D - CA^{-1}B$ being the Schur complement. In this context A acts on the displacement and Kirchhoff stress, while D acts on the pressure. Interpreting the inverse of a matrix as the action of solving a linear system involving the original matrix, this block Gaussian elimination then reduces the problem of solving the coupled preconditioned system to that of solving two separate smaller linear systems involving matrices $\hat{A}$ and $\hat{S}$. As a result, the availability of fast approximate solvers for the two smaller linear problems is crucial to the performance of the preconditioner.

Even if a robust approximation for the top-left block A is known, approximating the Schur complement S is usually a challenging task, as it is typically dense [9]. An augmented Lagrangian approach which effectively controls the Schur complement for the Oseen problem was introduced in [9]. The idea is to introduce an extra term in the variational formulation that does not affect the overall continuous solution, but serves to ease the approximation of the Schur complement [20]. This extra augmentation is weighted by a positive constant γ, and is often regarded as the penalty term enforcing the constraint in the problem. Adding the augmented term leads to changes in the linear system, in particular changes to the blocks of the matrix $\mathcal{A}$, with $\hat{A}_\gamma$ and $\hat{S}_\gamma$ being the augmented versions of $\hat{A}$ and $\hat{S}$; by increasing the penalty parameter γ, $\hat{S}_\gamma$ becomes a better and better approximation to S_γ, at the cost of making the operator A_γ more complex. In our context, the augmented Lagrangian strategy allows us to apply direct factorisations to A_γ instead of $\mathcal{A}$, substantially decreasing time to solution.

The outline of the paper is as follows. Section 2 summarises the equations of hyperelasticity for general constitutive laws, and presents the continuous form of the three-field version of the problem in strong and weak forms. In Section 3 we address the linearisation of the weak form and sketch its solvability analysis when restricted to neo-Hookean materials. There we also discuss the minimisation of the general nonlinear variational form. A mixed finite element discretisation and the construction of an augmented Lagrangian preconditioner are detailed in Section 4. We numerically examine the properties of the formulation, the finite element scheme, and of the preconditioner in Section 5. We conclude in Section 6 with a brief summary of our findings and also discussing ongoing extensions of this work.

2 Model description

2.1 Kinematics and constitutive relations

Let $\Omega \subset \mathbb{R}^d$ ($d \in \{2,3\}$) denote an open, connected Lipschitz domain with piecewise smooth boundary $\partial\Omega$, representing a deformable body in its reference configuration, and denote by $\boldsymbol{n}$ the outward unit normal vector on $\partial\Omega$. The kinematic description of finite deformations is made precise as follows. A material point in Ω is denoted by $\boldsymbol{x}$, whereas $\mathbf{U} : \Omega \to \mathbb{R}^d$ will denote the displacement field defining its new position $\boldsymbol{x} + \mathbf{U}(\boldsymbol{x})$ in the deformed configuration. The tensor $\mathbf{F} := \mathbf{I} + \nabla\mathbf{U}$ is the gradient (applied with respect to the fixed material coordinates) of the deformation map; its Jacobian determinant, denoted by $J = \det\mathbf{F} = \det(\mathbf{I} + \nabla\mathbf{U})$, measures the solid volume change during the deformation; and $\mathbf{C} = \mathbf{F}^{\mathtt{t}}\mathbf{F}$ is the right Cauchy-Green deformation tensor on which all strain measures will be based (here the superscript $(\cdot)^{\mathtt{t}}$ denotes the transpose operator). The triplet $(\boldsymbol{f}_0(\boldsymbol{x}), \boldsymbol{s}_0(\boldsymbol{x}), \boldsymbol{n}_0(\boldsymbol{x}))$ represents a coordinate system pointing in the local preferential directions of motion with $\boldsymbol{n}_0(\boldsymbol{x}) = \boldsymbol{f}_0(\boldsymbol{x}) \times \boldsymbol{s}_0(\boldsymbol{x})$, and the system is restricted to $(\boldsymbol{f}_0(\boldsymbol{x}), \boldsymbol{s}_0(\boldsymbol{x}))$ in 2D. The first isotropic invariant ruling deviatoric effects is $I_1(\mathbf{C}) = \mathbf{tr}\,\mathbf{C}$, and for generic unit vectors $\boldsymbol{f}_0, \boldsymbol{s}_0$, the scalars $I_{4,f}(\mathbf{C}) = \boldsymbol{f}_0 \cdot (\mathbf{C}\boldsymbol{f}_0)$, $I_{4,s}(\mathbf{C}) = \boldsymbol{s}_0 \cdot (\mathbf{C}\boldsymbol{s}_0)$, $I_{8,fs}(\mathbf{C}) = \boldsymbol{f}_0 \cdot (\mathbf{C}\boldsymbol{s}_0)$ are direction-dependent pseudo-invariants of $\mathbf{C}$ measuring direction-specific stretches.

Constitutive relations depend on the specific material under consideration and they are encoded through a strain energy density function Ψ written in terms of the deformation gradient. We consider two cases: the generic neo-Hookean material law and the Holzapfel–Ogden law specifically designed for orthotropic myocardial tissue [24]. The strain energy densities read respectively

$$\Psi_{\mathrm{NH}}(\mathbf{F}) = \frac{\mu}{2}(I_1 - d), \quad \Psi_{\mathrm{HO}}(\mathbf{F}) = \frac{a}{2b}e^{b(I_1-d)} + \frac{a_{fs}}{2b_{fs}}\left[e^{b_{fs}I_{8,fs}^2} - 1\right] + \sum_{i\in\{f,s\}}\frac{a_i}{2b_i}\left[e^{b_i(I_{4,i}-1)_+^2} - 1\right], \quad (2.1)$$

where $\mu,\ a, b, a_i, b_i$ with $i \in \{f, s, fs\}$ are material parameters and we have used the notation $(s)_+ := s$ if $s > 0$ or zero otherwise. Both specifications in (2.1) satisfy the condition of polyconvexity needed for minimisers of the free potential energy form of the problem to exist [30].

The first Piola–Kirchhoff stress tensor is

$$\mathbf{P} = \frac{\partial\Psi_{(\cdot)}}{\partial\nabla\mathbf{U}} - P(\mathbf{I} + \nabla\mathbf{U})^{-\mathtt{t}}, \quad (2.2)$$

where P denotes the solid hydrostatic pressure, which is the Lagrange multiplier used to impose the incompressibility constraint

$$\det(\mathbf{I} + \nabla\mathbf{U}) = 1,$$

and which implies that J does not appear in (2.2). The symmetric Kirchhoff stress tensor is given by

$$\boldsymbol{\Pi} = \mathbf{P}\mathbf{F}^{\mathtt{t}} = \frac{\partial\Psi_{(\cdot)}}{\partial\nabla\mathbf{U}}(\mathbf{I} + \nabla\mathbf{U})^{\mathtt{t}} - P\mathbf{I}. \quad (2.3)$$

2.2 Force balance and boundary conditions

The constitutive relation, the balance of linear momentum, and the incompressibility constraint are then combined (when posed in the inertial reference frame and under static mechanical equilibrium configuration) in the following strong form

$$\boldsymbol{\Pi} - \frac{\partial\Psi_{(\cdot)}}{\partial\nabla\mathbf{U}}(\mathbf{I} + \nabla\mathbf{U})^{\mathtt{t}} + P\mathbf{I} = \mathbf{0} \quad \text{in } \Omega, \quad (2.4a)$$

$$-\mathbf{div}\ \boldsymbol{\Pi}(\mathbf{I} + \nabla\mathbf{U})^{-\mathtt{t}} = \rho_0\boldsymbol{b} \quad \text{in } \Omega, \quad (2.4b)$$

$$\det(\mathbf{I} + \nabla\mathbf{U}) - 1 = 0 \quad \text{in } \Omega, \quad (2.4c)$$

where ρ_0 is the reference medium density and $\boldsymbol{b}$ is a vector field of body loads. The balance of angular momentum translates into the condition of symmetry of the Kirchhoff stress tensor and it is implicitly carried by the momentum and constitutive relations.

The Euler-Lagrange equations (2.4) will be supplemented with mixed displacement and traction boundary conditions

$$\mathbf{U} = \mathbf{0} \quad \text{on} \quad \partial\Omega_D, \qquad \text{and} \qquad \mathbf{\Pi}(\mathbf{I} + \nabla\mathbf{U})^{-\mathsf{t}}\boldsymbol{n} = \boldsymbol{t} \quad \text{on} \quad \partial\Omega_N, \tag{2.5}$$

where $\partial\Omega_D$,$\partial\Omega_N$ are a disjoint partition of the boundary $\partial\Omega$ and $\boldsymbol{t}$ is a prescribed traction. We assume that both $\boldsymbol{b}$ and $\boldsymbol{t}$ are sufficiently regular.

2.3 Three-field weak formulation

We proceed to test (2.4a)-(2.4c) against suitable functions, integrating by parts only in (2.4b), and using (2.5), to obtain the following nonlinear variational problem: Find $(\mathbf{\Pi}, \mathbf{U}, P) \in \mathbb{L}^4_{\mathrm{sym}}(\Omega) \times \mathbf{W}^{1,4}_D(\Omega) \times \mathrm{L}^4(\Omega)$ such that

$$\int_\Omega \left[\mathbf{\Pi} - \frac{\partial\Psi}{\partial\nabla\mathbf{U}}(\mathbf{I} + \nabla\mathbf{U})^{\mathsf{t}} + P\mathbf{I}\right] : \boldsymbol{\tau} = 0 \qquad \forall \boldsymbol{\tau} \in \mathbb{L}^4_{\mathrm{sym}}(\Omega), \tag{2.6a}$$

$$\int_\Omega \mathbf{\Pi}(\mathbf{I} + \nabla\mathbf{U})^{-\mathsf{t}} : \nabla\boldsymbol{v} = \int_\Omega \rho_0\boldsymbol{b}\cdot\boldsymbol{v} + \int_{\partial\Omega_N} \boldsymbol{t}\cdot\boldsymbol{v} \qquad \forall \boldsymbol{v} \in \mathbf{H}^1_D(\Omega), \tag{2.6b}$$

$$\int_\Omega [\det(\mathbf{I} + \nabla\mathbf{U}) - 1]\, q = 0 \qquad \forall q \in \mathrm{L}^4(\Omega), \tag{2.6c}$$

where $\mathbb{L}^4_{\mathrm{sym}}(\Omega) := \{\boldsymbol{\tau} \in \mathbb{L}^4(\Omega) : \boldsymbol{\tau} = \boldsymbol{\tau}^{\mathsf{t}}\}$, $\mathbf{W}^{1,4}_D(\Omega) = \{\boldsymbol{v} \in \mathbf{W}^{1,4}(\Omega) : \boldsymbol{v} = \mathbf{0} \text{ on } \partial\Omega_D\}$, and $\mathbf{H}^1_D(\Omega) = \{\boldsymbol{v} \in \mathbf{H}^1(\Omega) : \boldsymbol{v} = \mathbf{0} \text{ on } \partial\Omega_D\}$. We have taken the usual notation for tensor-tensor scalar product $\boldsymbol{\sigma} : \boldsymbol{\tau} = \mathbf{tr}(\boldsymbol{\sigma}^{\mathsf{t}}\boldsymbol{\tau})$, and we are implicitly assuming that the displacements are admissible in the sense that they have sufficient regularity as made precise above, or they are in $\mathbf{W}^{1,d}(\Omega)$ and they satisfy $\det(\mathbf{I} + \nabla\mathbf{U}) > 0$ (which implies that deformations are continuous), see e.g. [8, 17, 40].

The motivation for using three-field elasticity formulations is to avoid volumetric locking [27], and to provide direct approximation of a variable of importance [33, 36], nonetheless at a higher computational cost. As mentioned in [16], capturing stress concentrations with the guarantee of stress convergence under mesh refinement is a key requirement that is very difficult to achieve in a point-wise manner simply by standard displacement-based formulations. A further advantage of using the Kirchhoff stress is that this tensor is symmetric and for simpler material laws is a polynomial function of the displacements, whereas first and second Piola–Kirchhoff stresses are rational functions of displacement [15].

2.4 Energy minimisation and an augmented Lagrangian form

Regarding the general case of nonlinear elasticity, let us denote by $\mathbb{M}^3$ the set of all 3×3 matrices, and

$$\mathbb{M}^3_+ = \{\mathbf{A} \in \mathbb{M}^3 : \det(\mathbf{A}) > 0\}.$$

A stored energy function $\Psi : \mathbb{M}^3_+ \to \mathbb{R}$ is said to be polyconvex if there exists a convex function $G : \mathbb{M}^3 \times \mathbb{M}^3 \to \mathbb{R}$ such that

$$\Psi(\mathbf{F}) = G(\mathbf{F}, \operatorname{adj}\mathbf{F}), \quad \mathbf{F} \in \mathbb{M}^3_+.$$

The function G is coercive if there exist $a \in \mathbb{R}$, $b > 0$, $p \geq 2$, and $q \geq \frac{p}{p-1}$ such that

$$G(\mathbf{F}, \mathbf{H}) \geq a + b(\|\mathbf{F}\|^p + \|\mathbf{H}\|^q), \quad (\mathbf{F}, \mathbf{H}) \in \mathbb{M}^3 \times \mathbb{M}^3,$$

where $\|\mathbf{F}\|$ is the Euclidean norm of the matrix $\mathbf{F} \in \mathbb{R}^{3\times3}$.

According to the right-hand side of (2.6b), let the linear functional M be defined by

$$M(\boldsymbol{v}) = \int_\Omega \rho_0\boldsymbol{b}\cdot\boldsymbol{v} + \int_{\partial\Omega_N} \boldsymbol{t}\cdot\boldsymbol{v}\,,$$

which gives the external force to the system. Recall that the standard energy approach for nonlinear elasticity is to find the solution of the minimisation problem

$$\frac{1}{2}\int_\Omega \Psi(\mathbf{I}+\nabla\mathbf{U}) - M(\mathbf{U}), \tag{2.7}$$

over a suitable space for displacements [4, 39]. Existence of a solution of the minimisation problem using pure Dirichlet boundary conditions has been proved in [3, 44], and we recall here its application to (2.4).

Theorem 2.1 *Let the stored energy function* $\Psi : \mathbb{M}^3_+ \to \mathbb{R}$ *be continuous and polyconvex with* $\Psi(\mathbf{F}) = G(\mathbf{F}, \operatorname{adj}\mathbf{F})$ *on* $\mathbb{M}^3_+$*, with* G *coercive. Let* $\boldsymbol{b} \in \mathbf{L}^{\frac{p}{p-1}}(\Omega)$ *and suppose that the set*

$$\Sigma = \{\boldsymbol{v} \in \mathbf{W}^{1,p}(\Omega) : \operatorname{adj}(\nabla\boldsymbol{v}) \in \mathbb{L}^q(\Omega, M^3_+),\ \det(\nabla\boldsymbol{v}) = 1 \text{ a.e. in } \Omega, \quad \boldsymbol{v} = \boldsymbol{g} \text{ on } \partial\Omega\},$$

is not empty. Assume further that the total stored energy function $S : \Sigma \to \mathbb{R}$ *defined by*

$$S(\boldsymbol{v}) = \int_\Omega \Psi(\nabla\boldsymbol{v}) - M(\boldsymbol{v}),$$

satisfies

$$\inf_{\boldsymbol{v}\in\Sigma} S(\boldsymbol{v}) < \infty.$$

Then the problem of finding $\mathbf{U}$ *such that*

$$\mathbf{U} \in \Sigma \quad \text{and} \quad S(\mathbf{U}) = \inf_{\boldsymbol{v}\in\Sigma} S(\boldsymbol{v}),$$

has at least one solution.

Using the three unknowns from our formulation we can recast the standard minimisation problem as a constrained minimisation of (2.7) subject to the constraints

$$\begin{aligned}\mathbf{\Pi} &= \frac{\partial\Psi(\mathbf{I}+\nabla\mathbf{U})}{\partial(\mathbf{I}+\nabla\mathbf{U})}(\mathbf{I}+\nabla\mathbf{U})^{\mathtt{t}} - p\mathbf{I},\\ \det(\mathbf{I}+\nabla\mathbf{U}) &= 1.\end{aligned}$$

On the other hand, an augmented Lagrangian formulation is obtained by including a constraint in the minimisation formulation and writing the constraints in weak form. Therefore we minimise the functional

$$\frac{1}{2}\int_\Omega \Psi(\mathbf{I}+\nabla\mathbf{U}) + \gamma\|\det(\mathbf{I}+\nabla\mathbf{U}) - 1\|^2_{0,\Omega} - M(\mathbf{U}), \tag{2.8}$$

(where $\gamma \geq 0$ is the augmentation parameter that also influences the convergence of nonlinear solvers), subject to the constraints defined by equations (2.6a) and (2.6c).

Therefore the constrained minimisation results in the modified Euler-Lagrange equations

$$\int_\Omega \left[\mathbf{\Pi} - \frac{\partial\Psi}{\partial\nabla\mathbf{U}}(\mathbf{I}+\nabla\mathbf{U})^{\mathtt{t}} + p\mathbf{I}\right] : \boldsymbol{\tau} = 0 \qquad \forall\boldsymbol{\tau} \in \mathbb{L}^4_{\mathrm{sym}}(\Omega), \tag{2.9a}$$

$$\int_\Omega \mathbf{\Pi}(\mathbf{I}+\nabla\mathbf{U})^{-\mathtt{t}} : \nabla\boldsymbol{v} + \gamma\int_\Omega [\det(\mathbf{I}+\nabla\mathbf{U}) - 1][\det(\mathbf{I}+\nabla\boldsymbol{v}) - 1] = M(\boldsymbol{v}) \qquad \forall\boldsymbol{v} \in \mathbf{H}^1_D(\Omega), \tag{2.9b}$$

$$\int_\Omega [\det(\mathbf{I}+\nabla\mathbf{U}) - 1]\, q = 0 \qquad \forall q \in \mathrm{L}^4(\Omega). \tag{2.9c}$$

3 Consistent linearisation and solvability

Apart from the discussion in Section 2.4, we do not address in detail the solvability of (2.4), but rather refer to the literature complementing the general theory for well-posedness of hyperelasticity found in e.g. [29, 30]. Nevertheless, we briefly address some properties of the Fréchet derivative of the solution operator to the original problem, at a smooth regular exact solution.

3.1 Definition

Consider the following set of coupled PDEs written in mixed form, and arising from a Newton–Raphson linearisation of the equations of hyperelasticity in weak form (2.6): Starting from a sufficiently regular initial guess $(\mathbf{\Pi}^{k=0}, \mathbf{U}^{k=0}, P^{k=0})$, for $k = 0, 1, \ldots$, find stress, displacement and pressure increments $(\boldsymbol{\pi}^{k+1}, \boldsymbol{u}^{k+1}, p^{k+1})$ such that

$$\int_\Omega \left[\boldsymbol{\pi}^{k+1} - 2\ \mathrm{sym}\left(\frac{\partial \Psi^k}{\partial \mathbf{F}^k}(\nabla \boldsymbol{u}^{k+1})^{\mathtt{t}}\right) + p^{k+1}\mathbf{I}\right] : \boldsymbol{\tau} = \int_\Omega \boldsymbol{\mathcal{R}}^k_{\mathbf{\Pi}} : \boldsymbol{\tau} \qquad \forall \boldsymbol{\tau} \in \mathbb{L}^2_{\mathrm{sym}}(\Omega), \tag{3.1a}$$

$$\int_\Omega \left[\boldsymbol{\pi}^{k+1}(\mathbf{F}^k)^{-\mathtt{t}} - \mathbf{\Pi}^k(\mathbf{F}^k)^{-\mathtt{t}}[\nabla \boldsymbol{u}^{k+1}]^{\mathtt{t}}(\mathbf{F}^k)^{-\mathtt{t}}\right] : \nabla \boldsymbol{v} = \int_\Omega \boldsymbol{\mathcal{R}}^k_{\mathbf{U}} \cdot \boldsymbol{v} \qquad \forall \boldsymbol{v} \in \mathbf{H}^1_D(\Omega), \tag{3.1b}$$

$$\int_\Omega \left(J^k(\mathbf{F}^k)^{-\mathtt{t}} : \nabla \boldsymbol{u}^{k+1}\right) q = \int_\Omega \mathcal{R}^k_P q \qquad \forall q \in \mathrm{L}^2(\Omega), \tag{3.1c}$$

then update

$$\mathbf{\Pi}^{k+1} = \mathbf{\Pi}^k + \boldsymbol{\pi}^{k+1}, \quad \mathbf{U}^{k+1} = \mathbf{U}^k + \boldsymbol{u}^{k+1}, \quad P^{k+1} = P^k + p^{k+1},$$

and stop once either the increments or the residuals, in absolute or relative norms, drop below a given tolerance.

Here $\boldsymbol{\mathcal{R}}^k_{\mathbf{\Pi}}, \boldsymbol{\mathcal{R}}^k_{\mathbf{U}}, \mathcal{R}^k_P$ are tensor, vector, and scalar residuals associated with the Newton–Raphson linearisation at the previous step k (including the body load term), and we have used the auxiliary notation $\mathbf{F}^k = \mathbf{I} + \nabla \mathbf{U}^k$, $J^k = \det \mathbf{F}^k$ and $\mathrm{sym}(\boldsymbol{\tau}) = (\boldsymbol{\tau} + \boldsymbol{\tau}^{\mathtt{t}})/2$ for a given tensor $\boldsymbol{\tau}$. These terms are supposed to be regular enough. In (3.1b)-(3.1c) we have also used the following relations that arise from taking the Gâteaux derivatives of the solution operator in the direction of the displacement increments $\boldsymbol{u}$

$$\frac{\mathrm{d}}{\mathrm{d}\nabla \mathbf{U}}(\mathbf{I} + \nabla \mathbf{U})^{-\mathtt{t}}\big|_{\boldsymbol{u}} = -(\mathbf{F}^k)^{-\mathtt{t}}[\nabla \boldsymbol{u}]^{\mathtt{t}}(\mathbf{F}^k)^{-\mathtt{t}},$$
$$\frac{\mathrm{d}}{\mathrm{d}\nabla \mathbf{U}} \det(\mathbf{I} + \nabla \mathbf{U})\big|_{\boldsymbol{u}} = J^k\left((\mathbf{F}^k)^{-\mathtt{t}} : \nabla \boldsymbol{u}\right)\mathbf{I}.$$

The boundary conditions associated with the linearisation of the strong form (2.4) translate into zero incremental displacement on $\partial\Omega_D$ and zero linearised normal stress on $\partial\Omega_N$. Note also that in (3.1a)-(3.1c) the incremental solutions should now possess the following regularity

$$(\boldsymbol{\pi}^{k+1}, \boldsymbol{u}^{k+1}, p^{k+1}) \in \mathbb{L}^2_{\mathrm{sym}}(\Omega) \times \mathbf{H}^1_D(\Omega) \times \mathrm{L}^2(\Omega).$$

Using the strong form of (3.1a) and the symmetry of $\boldsymbol{\tau}$ we can write

$$\nabla \boldsymbol{u}^{k+1} = \left[2\frac{\partial \Psi^k}{\partial \mathbf{F}^k}\right]^{-1}(\boldsymbol{\pi}^{k+1} + p^{k+1}\mathbf{I} - \boldsymbol{\mathcal{R}}^k_{\mathbf{\Pi}}), \tag{3.2}$$

which implies that it is possible to rewrite (3.1c) as follows

$$\int_\Omega \left(J^k(\mathbf{F}^k)^{-\mathtt{t}} : \left[2\frac{\partial \Psi^k}{\partial \mathbf{F}^k}\right]^{-1}(\boldsymbol{\pi}^{k+1} + p^{k+1}\mathbf{I})\right) q = \int_\Omega \mathcal{R}^k_P q + \int_\Omega \left(J^k(\mathbf{F}^k)^{-\mathtt{t}} : \left[2\frac{\partial \Psi^k}{\partial \mathbf{F}^k}\right]^{-1} \boldsymbol{\mathcal{R}}^k_{\mathbf{\Pi}}\right) q \quad \forall q \in \mathrm{L}^2(\Omega). \tag{3.3}$$

As in [26, 31] one can suppose that after each Newton step the quantities from the previous iteration and the overall residuals have enough regularity so that the integrals in (3.3) are well-defined.

We cannot continue much further without specifying the form of the strain energy density. In order to make ideas more precise we will focus in the rest of the section on the case of neo-Hookean materials defined by Ψ_{NH} (cf. (2.1)). Then, for the term in (2.6a), we have

$$\frac{\partial \Psi_{\mathrm{NH}}}{\partial \nabla \mathbf{U}} = \mu(\mathbf{I} + \nabla \mathbf{U}).$$

Moreover, the linearisation procedure was done starting from a generic initial guess of the Newton iterates. In case one commences with the stress-free and motionless initial guess, that is,

$$(\boldsymbol{\Pi}^{k=0}, \mathbf{U}^{k=0}, P^{k=0}) = (\mathbf{0}, \mathbf{0}, 0), \tag{3.4}$$

we can simplify further by characterising the following bilinear forms and linear functionals

$$a_1(\boldsymbol{\pi}, \boldsymbol{\tau}) = \frac{1}{2\mu}\int_\Omega \boldsymbol{\pi} : \boldsymbol{\tau}, \quad a_3(p, q) = \frac{d}{2\mu}\int_\Omega pq, \quad b_1(\boldsymbol{u}, \boldsymbol{\tau}) = -\int_\Omega \nabla \boldsymbol{u} : \boldsymbol{\tau}, \quad b_2(p, \boldsymbol{\tau}) = \frac{1}{2\mu}\int_\Omega p\ \mathbf{tr}(\boldsymbol{\tau}),$$
$$F_1(\boldsymbol{\tau}) = \int_\Omega \boldsymbol{\mathcal{R}}_{\boldsymbol{\Pi}} : \boldsymbol{\tau}, \quad F_2(\boldsymbol{v}) = \int_\Omega \boldsymbol{\mathcal{R}}_{\mathbf{U}} \cdot \boldsymbol{v}, \quad F_3(q) = \int_\Omega \mathcal{R}_P q + \frac{1}{2\mu}\int_\Omega \mathbf{tr}\,\boldsymbol{\mathcal{R}}_{\boldsymbol{\Pi}}\, q,$$

so that the first iteration of (3.1) (for a neo-Hookean material) reduces to the symmetric variational problem: Find $(\boldsymbol{\pi}, \boldsymbol{u}, p) \in \mathbb{L}^2_{\mathrm{sym}}(\Omega) \times \mathbf{H}^1_D(\Omega) \times \mathrm{L}^2(\Omega)$ such that

$$\begin{aligned} a_1(\boldsymbol{\pi}, \boldsymbol{\tau}) + b_1(\boldsymbol{u}, \boldsymbol{\tau}) + b_2(p, \boldsymbol{\tau}) &= F_1(\boldsymbol{\tau}) \quad \forall \boldsymbol{\tau} \in \mathbb{L}^2_{\mathrm{sym}}(\Omega), \\ b_1(\boldsymbol{v}, \boldsymbol{\pi}) &= F_2(\boldsymbol{v}) \quad \forall \boldsymbol{v} \in \mathbf{H}^1_D(\Omega), \\ b_2(q, \boldsymbol{\pi}) + a_3(p, q) &= F_3(q) \quad \forall q \in \mathrm{L}^2(\Omega), \end{aligned} \tag{3.5}$$

where we have dropped the iteration index and employed the symmetry of $\boldsymbol{\tau}$. We recall that in displacement-pressure formulations for hyperelasticity one also ends up with symmetric tangent problems (see e.g. [6,29]).

The system (3.5) results from exploiting the linearised counterpart of (3.2), that is

$$\boldsymbol{\pi} - 2\mu\,\mathrm{sym}(\nabla \boldsymbol{u}) + p\mathbf{I} = \mathbf{M},$$

(which implies $\mathbf{tr}(\boldsymbol{\pi}) - 2\mu\,\mathrm{div}\,\boldsymbol{u} + d\,p = \mathbf{tr}\,\mathbf{M}$), where $\mathbf{M}$ contains any additional linearisation terms and therefore $(\mathbf{tr}\,\mathbf{M})\mathbf{I}$ is absorbed as part of $\boldsymbol{\mathcal{R}}_{\boldsymbol{\Pi}}$ and appears in $F_3(q)$, exactly as in (3.3). Otherwise, in the last equation in (3.5) instead of $b_2(q, \boldsymbol{\pi})$ and $a_3(p, q)$, we should have (as we do have in (3.1c)) a block associated with a bilinear form $b_3(\boldsymbol{u}, q) = \int_\Omega q\,\mathrm{div}\,\boldsymbol{u}$, which would make the problem not block-symmetric:

$$\begin{aligned} a_1(\boldsymbol{\pi}, \boldsymbol{\tau}) + b_1(\boldsymbol{u}, \boldsymbol{\tau}) + b_2(p, \boldsymbol{\tau}) &= F_1(\boldsymbol{\tau}) \quad \forall \boldsymbol{\tau} \in \mathbb{L}^2_{\mathrm{sym}}(\Omega), \\ b_1(\boldsymbol{v}, \boldsymbol{\pi}) &= F_2(\boldsymbol{v}) \quad \forall \boldsymbol{v} \in \mathbf{H}^1_D(\Omega), \\ b_3(\boldsymbol{u}, q) &= F_3(q) \quad \forall q \in \mathrm{L}^2(\Omega). \end{aligned} \tag{3.6}$$

Note also that system (3.6) corresponds to the weak form of the Navier equations written in terms of the Cauchy stress, the displacement, and the pressure

$$\begin{aligned} \boldsymbol{\pi} - 2\mu\,\mathrm{sym}(\nabla \boldsymbol{u}) + p\mathbf{I} &= \boldsymbol{\mathcal{R}}_{\boldsymbol{\Pi}}, \\ -\mathbf{div}\ \boldsymbol{\pi} &= \boldsymbol{\mathcal{R}}_{\mathbf{U}}, \\ \mathrm{div}\,\boldsymbol{u} &= \mathcal{R}_P. \end{aligned} \tag{3.7}$$

It is important to remark that if instead of the stress-free initial state (3.4) we take only a motionless state (representing for instance a residual stress present in the system, as typical in soft tissue applications), e.g.

$$(\boldsymbol{\Pi}^{k=0}, \mathbf{U}^{k=0}, P^{k=0}) = (\mathbf{I}, \mathbf{0}, 0),$$

then an additional term appears in (3.7), resulting in the system

$$\begin{aligned} \boldsymbol{\pi} - 2\mu\,\mathrm{sym}(\nabla \boldsymbol{u}) + p\mathbf{I} &= \boldsymbol{\mathcal{R}}_{\boldsymbol{\Pi}}, \\ -\mathbf{div}(\boldsymbol{\pi} - \nabla \boldsymbol{u}^{\mathtt{t}}) &= \boldsymbol{\mathcal{R}}_{\mathbf{U}}, \\ \mathrm{div}\,\boldsymbol{u} &= \mathcal{R}_P. \end{aligned} \tag{3.8}$$

And similarly as above, after defining the bilinear form

$$a_2(\boldsymbol{u}, \boldsymbol{v}) = \int_\Omega (\nabla \boldsymbol{u})^{\mathtt{t}} : \nabla \boldsymbol{v} = 2\int_\Omega \mathrm{sym}(\nabla \boldsymbol{u}) : \mathrm{sym}(\nabla \boldsymbol{v}) - \int_\Omega \nabla \boldsymbol{u} : \nabla \boldsymbol{v},$$

the weak forms (3.5) and (3.6) are modified as

$$\begin{aligned} a_1(\boldsymbol{\pi},\boldsymbol{\tau}) + b_1(\boldsymbol{u},\boldsymbol{\tau}) + b_2(p,\boldsymbol{\tau}) &= F_1(\boldsymbol{\tau}) \quad \forall \boldsymbol{\tau} \in \mathbb{L}^2_{\mathrm{sym}}(\Omega), \\ b_1(\boldsymbol{v},\boldsymbol{\pi}) + a_2(\boldsymbol{u},\boldsymbol{v}) &= F_2(\boldsymbol{v}) \quad \forall \boldsymbol{v} \in \mathbf{H}^1_D(\Omega), \\ b_2(q,\boldsymbol{\pi}) + a_3(p,q) &= F_3(q) \quad \forall q \in \mathrm{L}^2(\Omega), \end{aligned} \tag{3.9}$$

and

$$\begin{aligned} a_1(\boldsymbol{\pi},\boldsymbol{\tau}) + b_1(\boldsymbol{u},\boldsymbol{\tau}) + b_2(p,\boldsymbol{\tau}) &= F_1(\boldsymbol{\tau}) \quad \forall \boldsymbol{\tau} \in \mathbb{L}^2_{\mathrm{sym}}(\Omega), \\ b_1(\boldsymbol{v},\boldsymbol{\pi}) + a_2(\boldsymbol{u},\boldsymbol{v}) &= F_2(\boldsymbol{v}) \quad \forall \boldsymbol{v} \in \mathbf{H}^1_D(\Omega), \\ + b_3(\boldsymbol{u},q) &= F_3(q) \quad \forall q \in \mathrm{L}^2(\Omega), \end{aligned} \tag{3.10}$$

respectively.

3.2 Solvability analysis for a linearised and simplified problem

In this section we prove the well-posedness of (3.5). To that end, after simple computations we first observe that (3.5) can be rewritten as:

$$\begin{aligned} \widehat{a}_1(\boldsymbol{\pi},\boldsymbol{\tau}) + b_1(\boldsymbol{u},\boldsymbol{\tau}) + \frac{1}{2\mu}\int_\Omega \left(\frac{1}{d}\,\mathbf{tr}(\boldsymbol{\pi}) + p\right)\mathbf{tr}(\boldsymbol{\tau}) &= F_1(\boldsymbol{\tau}) \quad \forall \boldsymbol{\tau} \in \mathbb{L}^2_{\mathrm{sym}}(\Omega), \\ b_1(\boldsymbol{v},\boldsymbol{\pi}) &= F_2(\boldsymbol{v}) \quad \forall \boldsymbol{v} \in \mathbf{H}^1_D(\Omega), \\ \frac{1}{2\mu}\int_\Omega \left(\frac{1}{d}\,\mathbf{tr}(\boldsymbol{\pi}) + p\right) q &= \frac{1}{d}F_3(q) \quad \forall q \in \mathrm{L}^2(\Omega), \end{aligned}$$

with

$$\widehat{a}_1(\boldsymbol{\pi},\boldsymbol{\tau}) = \frac{1}{2\mu}\int_\Omega \boldsymbol{\pi}^{\mathtt{d}} : \boldsymbol{\tau}^{\mathtt{d}},$$

where, for a given tensor field $\boldsymbol{\tau}$, $\boldsymbol{\tau}^{\mathtt{d}}$ is its deviatoric part, that is, $\boldsymbol{\tau}^{\mathtt{d}} = \boldsymbol{\tau} - \frac{1}{d}\,\mathbf{tr}(\boldsymbol{\tau})\mathbf{I}$. For a given $c \in \mathbb{R}$, $(\boldsymbol{\pi},\boldsymbol{u},p) = (c\mathbf{I},\mathbf{0},-c)$ is a solution to the homogeneous version of (3.5), and as a result the system does not have a unique solution. To fix this from now on we seek the unknown $\boldsymbol{\pi}$ in $\mathbb{L}^2_{0,\mathrm{sym}}(\Omega)$, defined by

$$\mathbb{L}^2_{0,\mathrm{sym}}(\Omega) := \left\{ \boldsymbol{\tau} \in \mathbb{L}^2_{\mathrm{sym}}(\Omega) \,:\, \int_\Omega \mathbf{tr}(\boldsymbol{\tau}) = 0 \right\},$$

which satisfies $\mathbb{L}^2_{\mathrm{sym}}(\Omega) = \mathbb{L}^2_{0,\mathrm{sym}}(\Omega) \oplus \mathbb{R}\mathbf{I}$. Then, since $\mathbf{tr}(\mathbb{L}^2_{0,\mathrm{sym}}(\Omega)) = \mathrm{L}^2_0(\Omega)$, with

$$\mathrm{L}^2_0(\Omega) := \left\{ q \in \mathrm{L}^2(\Omega) \,:\, \int_\Omega q = 0 \right\},$$

satisfying $\mathrm{L}^2(\Omega) = \mathrm{L}^2_0(\Omega) \oplus \mathbb{R}$, we readily obtain that, after restricting the trial and test spaces associated with the unknown $\boldsymbol{\pi}$ to $\mathbb{L}^2_{0,\mathrm{sym}}(\Omega)$, (3.5) is equivalent to the problem: Find $(\boldsymbol{\pi},\boldsymbol{u}) \in \mathbb{L}^2_{0,\mathrm{sym}}(\Omega) \times \mathbf{H}^1_D(\Omega)$ such that

$$\begin{aligned} \widehat{a}_1(\boldsymbol{\pi},\boldsymbol{\tau}) + b_1(\boldsymbol{u},\boldsymbol{\tau}) &= F_1(\boldsymbol{\tau}) - \frac{1}{d}F_3(\mathbf{tr}(\boldsymbol{\tau})) \quad \forall \boldsymbol{\tau} \in \mathbb{L}^2_{0,\mathrm{sym}}(\Omega), \\ b_1(\boldsymbol{v},\boldsymbol{\pi}) &= F_2(\boldsymbol{v}) \quad \forall \boldsymbol{v} \in \mathbf{H}^1_D(\Omega). \end{aligned} \tag{3.11}$$

We prove that (3.11) is well-posed to prove the well-posedness of (3.5). To do that, we establish the following technical result.

Lemma 3.1 *There exists $C > 0$ such that*

$$\|\boldsymbol{\tau}^{\mathtt{d}}\|_{0,\Omega} \geq C\|\boldsymbol{\tau}\|_{0,\Omega},\ \forall \boldsymbol{\tau} \in Ker(b_1) := \{\boldsymbol{\tau} \in \mathbb{L}^2_{0,\mathrm{sym}}(\Omega) : \int_\Omega \nabla\boldsymbol{v} : \boldsymbol{\tau} = 0 \quad \forall\, \boldsymbol{v} \in \mathbf{H}^1_D(\Omega)\}. \tag{3.12}$$

Proof. We proceed similarly to the proof of [21, Lemma 2.3]. In fact, we let $\boldsymbol{\tau} \in \mathrm{Ker}(b_1)$ and observe that since $\int_\Omega \mathbf{tr}(\boldsymbol{\tau}) = 0$, there exists $\boldsymbol{z} \in \mathbf{H}^1_D(\Omega)$ such that (see [22, Corollary 2.4])

$$\mathrm{div}\, \boldsymbol{z} = -\,\mathbf{tr}(\boldsymbol{\tau}) \quad \text{in} \quad \Omega \quad \text{and} \quad \|\boldsymbol{z}\|_{1,\Omega} \leq C \|\,\mathbf{tr}(\boldsymbol{\tau})\|_{0,\Omega}.$$

It follows that

$$\|\,\mathbf{tr}(\boldsymbol{\tau})\|^2_{0,\Omega} = \int_\Omega \mathbf{tr}(\boldsymbol{\tau})\, \mathrm{div}\, \boldsymbol{z} = \int_\Omega \nabla \boldsymbol{z} : (\mathbf{tr}(\boldsymbol{\tau})\mathbf{I}).$$

Then, since $\mathbf{tr}(\boldsymbol{\tau})\mathbf{I} = d(\boldsymbol{\tau} - \boldsymbol{\tau}^{\mathtt{d}})$ and $\int_\Omega \nabla \boldsymbol{z} : \boldsymbol{\tau} = 0$, it readily follows that

$$\|\,\mathbf{tr}(\boldsymbol{\tau})\|^2_{0,\Omega} = \int_\Omega \nabla \boldsymbol{z} : \boldsymbol{\tau}^{\mathtt{d}} \leq \|\boldsymbol{z}\|_{1,\Omega} \|\boldsymbol{\tau}^{\mathtt{d}}\|_{0,\Omega} \leq C \|\,\mathbf{tr}(\boldsymbol{\tau})\|_{0,\Omega} \|\boldsymbol{\tau}^{\mathtt{d}}\|_{0,\Omega},$$

which together with the fact that $\|\boldsymbol{z}\|_{1,\Omega} \leq C\|\,\mathbf{tr}(\boldsymbol{\tau})\|_{0,\Omega}$, implies

$$\|\,\mathbf{tr}(\boldsymbol{\tau})\|_{0,\Omega} \leq C \|\boldsymbol{\tau}^{\mathtt{d}}\|_{0,\Omega}.$$

This estimate, and the identity $\|\boldsymbol{\tau}\|^2_{0,\Omega} = \|\boldsymbol{\tau}^{\mathtt{d}}\|^2_{0,\Omega} + \frac{1}{d}\|\,\mathbf{tr}(\boldsymbol{\tau})\|^2_{0,\Omega}$, imply the result. □

Now we are in position of proving the well-posedness of (3.5).

Theorem 3.1 *There exists a unique solution* $(\boldsymbol{\pi}, \boldsymbol{u}, p) \in \mathbb{L}^2_{0,\mathrm{sym}}(\Omega) \times \mathbf{H}^1_D(\Omega) \times \mathrm{L}^2(\Omega)$ *to* (3.5).

Proof. According to the above, in what follows we prove equivalently that problem (3.11) is well-posed by means of the Babuška-Brezzi theory.

We begin by noticing that the ellipticity of $\widehat{a}_1(\boldsymbol{\pi}, \boldsymbol{\tau})$ on $\mathrm{Ker}(b_1)$ is a direct consequence of Lemma 3.1. Now, given $\boldsymbol{v} \in \mathbf{H}^1_D(\Omega)$, we let $\tilde{\boldsymbol{\tau}} = -\mathrm{sym}(\nabla \boldsymbol{v})$ and observe that

$$\int_\Omega \mathbf{tr}(\tilde{\boldsymbol{\tau}}) = -\int_\Omega \mathrm{div}\, \boldsymbol{v} = -\int_{\partial\Omega} \boldsymbol{v} \cdot \boldsymbol{n} = 0,$$

which implies that $\tilde{\boldsymbol{\tau}} \in \mathbb{L}^2_{0,\mathrm{sym}}(\Omega)$. In addition, the well-known Korn and Poincaré inequalities (see, e.g., [13, Corollaries 9.2.22, 9.2.25 and Proposition 5.3.5]) imply that

$$\|\tilde{\boldsymbol{\tau}}\|_{0,\Omega} = \|\mathrm{sym}(\nabla \boldsymbol{v})\|_{0,\Omega} \geq C \|\boldsymbol{v}\|_{1,\Omega}. \tag{3.13}$$

Then observing that $\tilde{\boldsymbol{\tau}} : \nabla \boldsymbol{v} = -\tilde{\boldsymbol{\tau}} : \tilde{\boldsymbol{\tau}}$, it follows that

$$\sup_{\substack{\boldsymbol{\tau} \in \mathbb{L}^2_{0,\mathrm{sym}}(\Omega) \\ \boldsymbol{\tau} \neq \mathbf{0}}} \frac{b_1(\boldsymbol{v}, \boldsymbol{\tau})}{\|\boldsymbol{\tau}\|_{0,\Omega}} \geq \frac{b_1(\boldsymbol{v}, \tilde{\boldsymbol{\tau}})}{\|\tilde{\boldsymbol{\tau}}\|_{0,\Omega}} = \|\tilde{\boldsymbol{\tau}}\|_{0,\Omega}$$

which together with (3.13) implies that b_1 satisfies the required inf-sup condition, thus finishing the proof. □

We end this section by observing that if we employ the same techniques used to establish well-posedness of (3.9) to study (3.10), then the results hold under a restriction on the bulk modulus.

4 Mixed finite element scheme and preconditioner

4.1 A Galerkin method

Let us denote by $\mathcal{T}_h$ a regular partition of Ω into simplices (triangles or tetrahedra) K of maximum diameter h_K, and define the mesh size as $h := \max\{h_K : K \in \mathcal{T}_h\}$. The set of facets (the skeleton of the mesh) will be denoted $\mathcal{E}_h$. In the lowest-order case, the specific finite element method we choose here is based

on solving the discrete weak form of the hyperelasticity equations using piecewise constant approximations of the symmetric Kirchhoff stress tensor, piecewise linear approximation of displacements, and piecewise constant approximation of solid pressure. More generally, for $\ell \geq 0$ we use the finite dimensional spaces $\mathbb{H}_h \subset \mathbb{L}^2_{\mathrm{sym}}(\Omega)$, $\mathbf{V}_h \subset \mathbf{H}^1(\Omega)$, $Q_h \subset \mathrm{L}^2(\Omega)$ defined as follows:

$$\begin{aligned}
\mathbb{H}_h &:= \{\boldsymbol{\tau}_h \in \mathbb{L}^2_{\mathrm{sym}}(\Omega) : \boldsymbol{\tau}_h|_K \in \mathbb{P}_\ell(K)^{d\times d} \,\forall K \in \mathcal{T}_h\},\\
\mathbf{V}_h &:= \{\boldsymbol{v}_h \in \mathbf{H}^1(\Omega) : \boldsymbol{v}_h|_K \in \mathbb{P}_{\ell+1}(K)^d \,\forall K \in \mathcal{T}_h,\ \boldsymbol{v}_h|_{\partial\Omega_D} = \mathbf{0}\},\\
Q_h &:= \{q_h \in \mathrm{L}^2(\Omega) : q_h|_K \in \mathbb{P}_\ell(K) \,\forall K \in \mathcal{T}_h\},
\end{aligned} \tag{4.1}$$

where $\mathbb{P}_r(R)$ denotes the space of polynomial functions of degree $s \leq r$ defined on the set R.

The Galerkin scheme associated with (3.9) is then defined as

$$\begin{aligned}
a_1(\boldsymbol{\pi}_h, \boldsymbol{\tau}_h) + b_1(\boldsymbol{u}_h, \boldsymbol{\tau}_h) &+ b_2(p_h, \boldsymbol{\tau}_h) = F_1(\boldsymbol{\tau}_h) && \forall \boldsymbol{\tau}_h \in \mathbb{H}_h,\\
b_1(\boldsymbol{v}_h, \boldsymbol{\pi}_h) + a_2(\boldsymbol{u}_h, \boldsymbol{v}_h) &= F_2(\boldsymbol{v}_h) && \forall \boldsymbol{v}_h \in \mathbf{V}_h,\\
b_2(q_h, \boldsymbol{\pi}_h) &+ a_3(p_h, q_h) + \beta \sum_{e\in\mathcal{E}_h} \int_e h_e \,[\![p_h]\!]\,[\![q_h]\!] = F_3(q_h) && \forall q_h \in Q_h,
\end{aligned} \tag{4.2}$$

where the discrete spaces correspond to those defined in (4.1) and where β is a positive, pressure stabilisation parameter independent of the mesh size, required in this simplicial counterpart of the finite element method for quadrilaterals studied in [15]. The symbol $[\![q]\!]$ denotes the jump of the generic scalar field q over a given facet $e \in \mathcal{E}_h$.

4.2 An augmented Lagrangian preconditioner

The discrete form of the general tangent problem (3.1) can be written as

$$\mathcal{M}\begin{pmatrix}\boldsymbol{\pi}_h\\ \boldsymbol{u}_h\\ p_h\end{pmatrix} = \begin{bmatrix}\mathcal{A}_1 & \mathcal{B}_1 & \mathcal{B}_2\\ \tilde{\mathcal{B}}_1 & \mathcal{A}_2 & O\\ \tilde{\mathcal{B}}_2 & O & \mathcal{A}_3\end{bmatrix}\begin{pmatrix}\boldsymbol{\pi}_h\\ \boldsymbol{u}_h\\ p_h\end{pmatrix} = \begin{pmatrix}\mathcal{F}_1\\ \mathcal{F}_2\\ \mathcal{F}_3\end{pmatrix}. \tag{4.3}$$

In order to fit (4.3) into the preconditioning framework described previously in Section 1, it is desirable to rearrange $\mathcal{M}$ as a 2×2 block matrix. We therefore treat $(\boldsymbol{\pi}_h, \boldsymbol{u}_h)$ together as one field and p_h as another.

The linear system after splitting becomes

$$\mathcal{A}\begin{pmatrix}\boldsymbol{\mathcal{U}}_h\\ p_h\end{pmatrix} = \begin{pmatrix}\boldsymbol{\kappa}\\ \tilde{b}\end{pmatrix}, \tag{4.4}$$

where

$$\begin{bmatrix}A & B\\ C & D\end{bmatrix} := \mathcal{A}, \tag{4.5}$$

with A being a 2×2 block matrix, B being a 2×1 block matrix, C being a 1×2 block, $D = \mathcal{A}_3$, and

$$\boldsymbol{\mathcal{U}}_h = \begin{pmatrix}\boldsymbol{\pi}_h\\ \boldsymbol{u}_h\end{pmatrix}, \quad \boldsymbol{\kappa} = \begin{pmatrix}\mathcal{F}_1\\ \mathcal{F}_2\end{pmatrix}, \quad \tilde{b} = \mathcal{F}_3.$$

We recall that the constraint imposed on the mechanical problem is $J - 1 = 0$, so the augmentation added to the weak form of the variational formulation is the Fréchet derivative of the term

$$\frac{\gamma}{2}\int_\Omega (J-1)^2. \tag{4.6}$$

The larger the value we take for γ, the more we penalise violation of the constraint. In fact, if γ is taken large enough, it provides an alternative to the use of the Lagrange multiplier p for enforcing the constraint,

although the augmented Lagrangian approach is preferable to this pure penalty formulation. Following from the similar ideas in [19], the linear system (4.4) after discrete augmentation then becomes

$$\mathcal{A}_\gamma \begin{pmatrix} \boldsymbol{u}_h \\ p_h \end{pmatrix} = \begin{bmatrix} A_\gamma & B \\ C & D \end{bmatrix} \begin{pmatrix} \boldsymbol{u}_h \\ p_h \end{pmatrix} = \begin{pmatrix} \boldsymbol{\kappa} \\ \tilde{b} \end{pmatrix}, \tag{4.7}$$

where

$$A_\gamma = A + \gamma B M_p^{-1} C, \tag{4.8}$$

and M_p is the pressure mass matrix. We construct the preconditioner based on the block factorisation formula

$$\mathcal{P}^{-1} = \begin{bmatrix} I & -\hat{A}_\gamma^{-1} B \\ 0 & I \end{bmatrix} \begin{bmatrix} \hat{A}_\gamma^{-1} & 0 \\ 0 & \hat{S}_\gamma^{-1} \end{bmatrix} \begin{bmatrix} I & 0 \\ -C\hat{A}_\gamma^{-1} & I \end{bmatrix}. \tag{4.9}$$

The smaller sparse linear system associated with the top-left block $\hat{A}_\gamma$ (i.e. the approximation of A_γ) is solved directly by the standard LU factorisation. The dense Schur complement approximation $\hat{S}_\gamma$, on the other hand, requires more consideration. Following from the definition of the Schur complement, S_γ can be expressed as

$$\begin{aligned} S_\gamma &= D - C A_\gamma^{-1} B \\ &= D - C(A + \gamma B M_p^{-1}\ C)^{-1} B, \end{aligned} \tag{4.10}$$

and can be simplified by the Sherman-Morrison-Woodbury inverse formula [2]:

$$S_\gamma = D + (-(CA^{-1}B)^{-1} - \gamma M_p^{-1})^{-1}. \tag{4.11}$$

By increasing the value of γ we are able to capture the dominating term in the expression of S_γ. An adequate approximation $\hat{S}_\gamma$ is thus obtained simply by neglecting the dominated terms. The resulting Schur complement approximation is then given by

$$\begin{aligned} \hat{S}_\gamma &= D + (-\gamma M_p^{-1})^{-1} \\ &= -\frac{1}{\gamma} M_p + D. \end{aligned} \tag{4.12}$$

The processes of solving the separate linear systems associated with $\hat{A}_\gamma$ and $\hat{S}_\gamma$ are known as the inner solves, and the process of solving the overall coupled system after preconditioning is called the outer solve. We adopt a single GMRES iteration preconditioned by direct factorisations of $\hat{A}_\gamma$ and $\hat{S}_\gamma$ for the inner solves, and use standard FGMRES iteration for the outer solve [37].

5 Numerical examples

In this section we present a set of computational tests that serve as verification of the convergence of the mixed method in the linear and nonlinear cases. We also explore the applicability of the formulation in computing some benchmark solutions [7]. All routines have been implemented using the finite element libraries FEniCS [1] and Firedrake [34].

5.1 Accuracy verification

On the domain $\Omega = (0,1)^2$ we consider the following closed-form displacement and pressure solving the nonlinear problem (2.4)

$$\mathbf{U} = 0.1(y^2, y^3)^\mathsf{t}, \quad P = x^4 - y^4,$$

DoF	h	$\|\boldsymbol{\Pi} - \boldsymbol{\Pi}_h\|_{0,\Omega}$	rate	$\|\mathbf{U} - \mathbf{U}_h\|_{1,\Omega}$	rate	$\|P - P_h\|_{0,\Omega}$	rate
neo-Hookean with $\ell = 0$							
51	0.707	65.20	–	0.057	–	32.22	–
179	0.353	27.81	1.229	0.029	0.997	12.31	1.388
675	0.176	12.61	1.143	0.014	1.002	5.222	1.237
2,627	0.088	6.004	1.069	0.007	1.002	2.412	1.114
10,371	0.044	2.938	1.031	0.003	1.001	1.165	1.050
41,219	0.022	1.455	1.014	0.001	1.000	0.573	1.023
neo-Hookean with $\ell = 1$							
147	0.707	3.483	–	0.005	–	1.035	–
547	0.353	0.795	2.130	0.001	2.047	0.143	2.848
2,115	0.176	0.193	2.042	3.5e-4	2.012	0.023	2.624
8,323	0.088	0.047	2.014	8.7e-5	2.003	0.004	2.345
33,027	0.044	0.011	2.005	2.1e-5	2.001	0.001	2.143
131,587	0.022	0.004	2.001	5.1e-6	2.000	2.5e-4	2.056
Holzapfel–Ogden with $\ell = 0$							
51	0.707	0.966	–	0.058	–	0.512	–
179	0.353	0.434	1.154	0.029	0.992	0.213	1.259
675	0.176	0.198	1.133	0.014	1.012	0.093	1.191
2,627	0.088	0.093	1.084	0.007	1.009	0.043	1.115
10,371	0.044	0.045	1.045	0.004	1.005	0.021	1.059
41,219	0.022	0.022	1.022	0.002	1.003	0.010	1.029
Holzapfel–Ogden with $\ell = 1$							
147	0.707	0.164	–	0.006	–	0.088	–
547	0.353	0.041	2.007	0.001	2.001	0.021	2.074
2,115	0.176	0.010	1.999	3.7e-4	2.082	0.005	2.021
8,323	0.088	0.002	2.001	8.9e-5	2.062	0.001	2.007
33,027	0.044	6.3e-4	2.001	2.2e-5	2.025	3.2e-4	2.004
131,587	0.022	1.6e-4	1.999	5.2e-6	2.001	7.9e-5	2.002

Table 5.1: Test 1: Error history for Kirchhoff stress, displacement, and pressure; associated with the mixed finite element method using different polynomial degrees $\ell \in \{0, 1\}$ and for neo-Hookean and Holzapfel–Ogden material laws.

and $\boldsymbol{\Pi}$ is computed with these solutions using (2.3). We consider both neo-Hookean and Holzapfel–Ogden materials and prescribe the interpolant of the exact displacement on the whole boundary. The mean value of pressure is fixed through a real Lagrange multiplier. These solutions satisfy the incompressibility constraint, and the body load is manufactured from the exact solutions and (2.4b). The material parameter for the neo-Hookean energy is $\mu = 100$, whereas the model parameters for the Holzapfel–Ogden energy are

$$a = 0.496, \quad b = 0.041, \quad a_f = 0.193, \quad b_f = 0.176, \quad a_s = 0.123, \quad b_s = 0.209,$$
$$a_{fs} = 0.162, \quad b_{fs} = 0.166, \quad \boldsymbol{f}_0 = (1, 0)^{\mathsf{t}}, \quad \boldsymbol{s}_0 = (0, -1)^{\mathsf{t}}.$$

The stabilisation parameter in the neo-Hookean test is $\beta = 10^{-4}$ and in the Holzapfel–Ogden case is $\beta = 10^{-2}$.

We implement a Newton–Raphson method that stops whenever a residual absolute tolerance of 10^{-8} is attained, and where at each iteration the discrete version of the linear system (3.1) is solved with the Multifrontal Massively Parallel Sparse direct Solver (MUMPS). We then do uniform mesh refinement and on each level we compute errors between approximate and exact solutions and record the absolute errors and convergence rates in Table 5.1, which indicate optimal error decay for the first- and second-order cases.

We also conduct an experimental convergence test for the linearised Galerkin scheme (4.2). Now the exact solutions satisfying (3.8) are

$$\boldsymbol{u} = 0.1(y^2, y^3)^{\mathsf{t}}, \quad p = x^4 - y^4, \quad \boldsymbol{\pi} = 2\mu \mathrm{sym}(\nabla \boldsymbol{u}) - p\mathbf{I},$$

DoFs	h	$\|\boldsymbol{\pi}-\boldsymbol{\pi}_h\|_{0,\Omega}$	rate	$\|\boldsymbol{u}-\boldsymbol{u}_h\|_{1,\Omega}$	rate	$\|p-p_h\|_{0,\Omega}$	rate
Linear, block symmetric (4.2) with $\ell=0$							
51	0.707	22.87	–	0.051	–	13.86	–
179	0.353	9.849	1.216	0.025	0.996	5.632	1.299
675	0.176	4.503	1.129	0.012	1.000	2.466	1.192
2,627	0.088	2.151	1.066	0.006	1.000	1.148	1.103
10,371	0.044	1.052	1.032	0.003	1.000	0.553	1.052
41,219	0.022	0.525	1.016	0.001	1.000	0.272	1.026
164,355	0.011	0.259	1.008	8.0e-4	1.000	0.135	1.013
Linear, block symmetric (4.2) with $\ell=1$							
147	0.707	4.358	–	0.004	–	2.843	–
547	0.353	0.806	2.433	0.001	2.022	0.499	2.351
2,115	0.176	0.178	2.177	2.6e-4	2.013	0.107	2.225
8,323	0.088	0.042	2.075	6.5e-5	2.006	0.025	2.099
33,027	0.044	0.010	2.032	1.6e-5	2.003	0.006	2.043
131,587	0.022	0.002	2.015	4.1e-6	2.001	0.001	2.019

Table 5.2: Test 1: Error history for stress, displacement, and pressure in the linear regime (3.8), with $\beta = 10^{-4}$.

and the external load is $\boldsymbol{b} = -\frac{1}{\rho_0}\,\mathbf{div}(\boldsymbol{\pi} - \nabla \boldsymbol{u}^{\mathsf{t}})$. We again take $\mu = 100$ and the error history is displayed in Table 5.2, where we use $\beta = 10^{-4}$. We observe the expected rates of convergence. Unreported numerical experiments indicate that the discretisation of the nonsymmetric formulation arising from (3.10) obtains the same results.

5.2 Compression benchmark in 2D

We study the deformation of a rectangular block that undergoes a pressure load (here implemented as a traction) applied on the centre of the top edge. The domain is $\Omega = (0, 20) \times (0, 10)$ (in mm^2), the shear modulus is $\mu = 240.565/(2(1 + 0.4999))\,\mathrm{MPa}$ and the applied pressure is $P_0 = 400\,\mathrm{MPa}$. On the top surface we prescribe zero tangential displacement, on the bottom we set zero normal displacement, and on the vertical boundaries we impose zero traction. As in [7], we record the vertical displacement on the centre of the top boundary for different levels of mesh resolution, for different polynomial degrees, and different values of the stabilisation parameter. The results are portrayed in the right plot of Figure 5.1. We observe how the output converges to the value -5.63, which agrees with the results from [7]. We can also see that for the first and second-order methods, the value $\beta = 0.001$ performs best. In the higher-order case the result is insensitive to the stabilisation, while in the lowest-order case the convergence with e.g. $\beta = 0.1$ is very poor. The number of Newton iterations is not shown as it practically coincides in all cases, and it varies between 5-6 steps.

5.3 Compression test in 3D

We consider the example of a hollow cylinder deforming under compression and shear in 3D [26, Sect. 5.3.2]. As in the previous example we employ an isotropic and incompressible neo-Hookean material now with shear modulus $\mu = 50$, and consider a hollow cylinder of height 4 cm, inner radius 0.75 cm and outer radius 1 cm. The domain is discretised into 23,946 tetrahedral elements yielding, for the lowest-order scheme, a total of 180,134 DoFs. The stabilisation is set to $\beta = 0.1$. The surface defined by $z = 0$ is clamped and the surface at $z = 4$ undergoes an increasing deformation. In contrast with Test 2, here we apply an incremental load taking 10 intermediate steps and progressively reaching a maximal displacement on the top surface of magnitude 1.5, and acting only in the directions x and z, equally. On the inner and outer radii we prescribe zero traction. The deformations induced by shear are seen from Figure 5.2, where we plot Kirchhoff stress

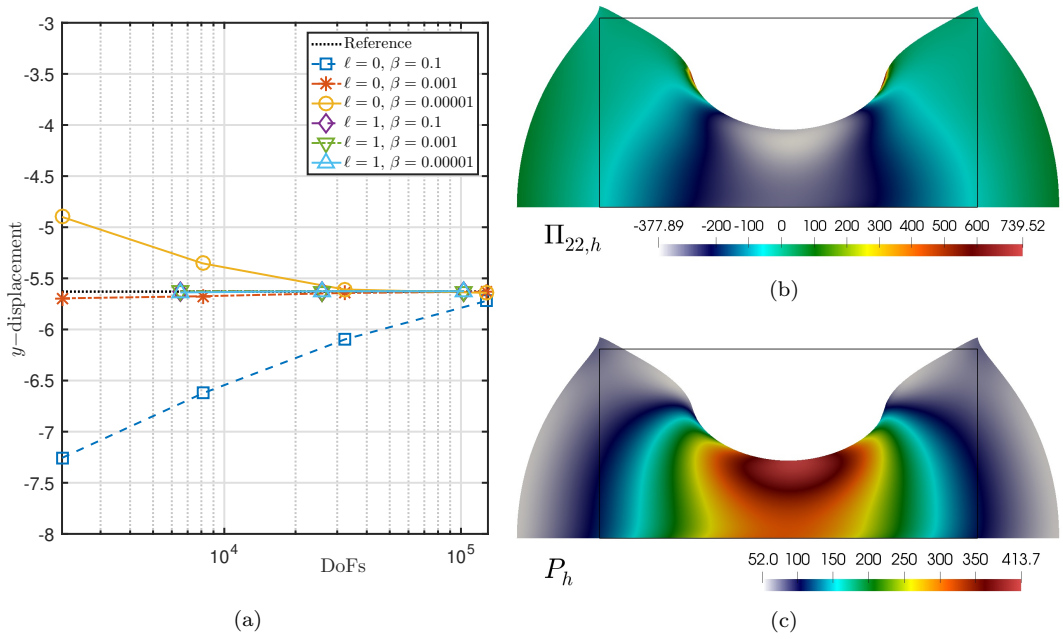

(a) (b) (c)

Figure 5.1: Test 2: compressing a neo-Hookean block. Left: vertical displacement on the top-centre of the domain according to the number of degrees of freedom and for different values of the pressure stabilisation. Right: $yy-$component of the Kirchhoff stress and pressure distribution plotted on the deformed configuration, computed with $\ell = 0$ and $\beta = 0.001$. For this case the displacement on the centre of the top edge is $\boldsymbol{u} = (0, -5.71)^{\mathsf{t}}$.

components and pressure on the deformed domain, showing the undeformed configuration with opacity. The overall behaviour of the simulation agrees with the results from [26].

5.4 Twist and contraction of left ventricle

Next we conduct a simple test on a patient-specific left ventricular geometry segmented from CT-scans. The basal region (the top surface) corresponds to $\partial\Omega_D$ where normal displacements are set to zero, whereas the epicardium and endocardium constitute $\partial\Omega_N$. On the endocardium we set an incremental traction increasing from $\mathbf{0}$ to $3\boldsymbol{n}$ (where $\boldsymbol{n}$ is the normal vector on the boundary), which represents the variation of endocardial pressure from zero to 3 kPa in a sub-stage of the ejection phase. On the epicardium we simply set zero traction. The directions of fibre and sheetlet orientation are generated with a Laplace-Dirichlet rule-based method in mixed form as described in [36], and the resulting muscle fibres have an orientation varying transmurally from the epicardial surface to the endocardial surface with a difference of 120 degrees, whereas the collagen sheetlets have a radial distribution relative to the ventricular centreline. This ventricular centreline is aligned with the $z-$axis, the apex-to-base distance is 10.13 cm, and the maximal circumferential radius is 3.94 cm. We generate a tetrahedral mesh of 94,269 cells and 22,193 vertices on which we implement the mixed scheme with $\ell = 1$ and $\beta = 50$. We employ the Holzapfel–Ogden material law with the constitutive parameters used in Example 1. The active contraction of the ventricle is incorporated through the so-called active strain approach (see e.g. [33]) where the activation function ξ is incremented together with the endocardial pressure up to a maximal activation of 12%. In order to achieve sufficient torsion and thickening of the ventricular wall, we also use an algebraic relation between the activation and the myocyte shortening that models sliding myofilaments of collagen and a transmurally heterogeneous activation that modulates different values of ξ in each direction (see details in [5, 35])

$$\xi_f = \xi, \quad \xi_n = (1-\zeta)k_0\xi + \zeta[(1-\xi)^{-1/2} - 1], \quad \xi_s = (1+\xi)^{-1}(1+\xi_n)^{-1} - 1,$$

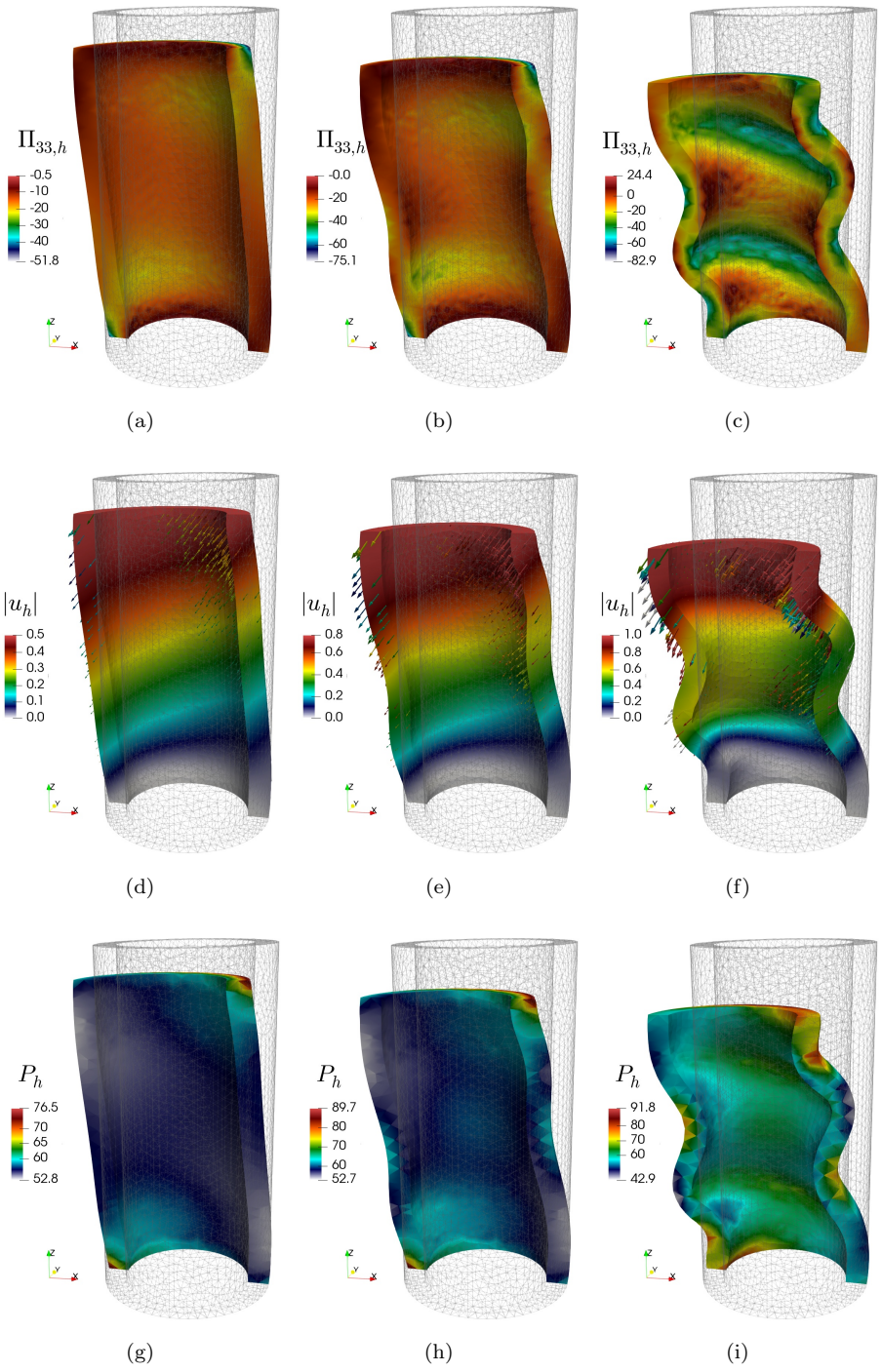

Figure 5.2: Test 3: compressing a neo-Hookean hollow cylinder for three incremental loadings (from left to right), using $\ell = 0$ and $\beta = 0.1$. Top: $zz-$component of the Kirchhoff stress. Middle: displacement magnitude and arrows. Bottom: pressure distribution plotted on the deformed configuration.

where ζ is a smooth indicator function going from 0 on the endocardium to 1 on the epicardium, and we choose a mild orthotropic activation parameter of $k_0 = 3$.

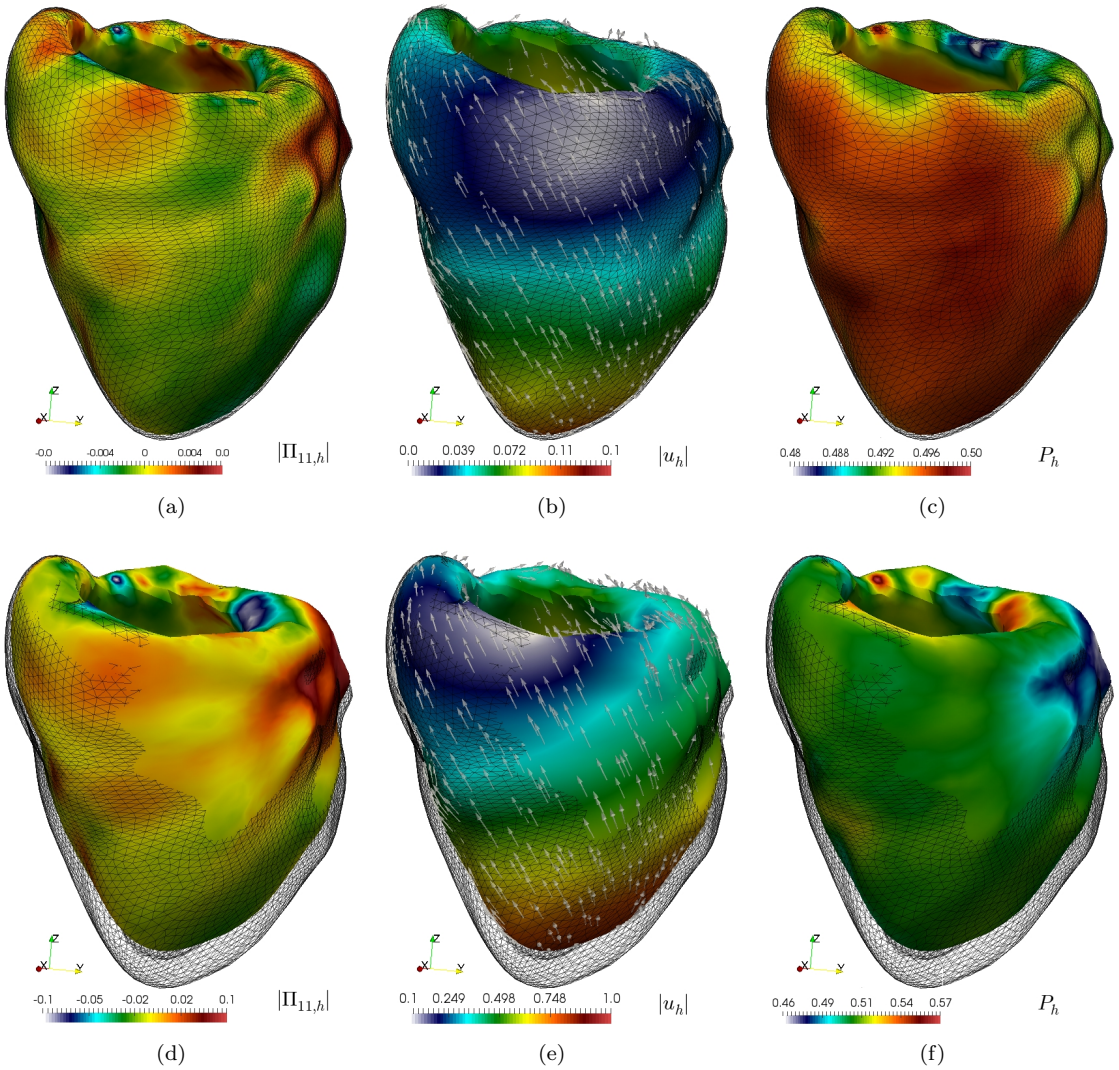

Figure 5.3: Test 4: contraction of an orthotropic cardiac ventricle for two and seven incremental steps of active strain loading (top and bottom, respectively). The Holzapfel–Ogden material law has been used. Left: $xx-$ component of the Kirchhoff stress. Middle: displacement magnitude and arrows. Right: pressure distribution plotted on the deformed configuration.

In Figure 5.3 we plot two snapshots of the obtained solutions, one at the beginning of the diastolic phase and the second one for the end-diastolic configuration. Stresses and pressure concentrate in the vicinity of the interface between the basal region and the endocardium, and we see the expected apex-to-base contraction together with a deformation following the fibre orientation and producing a more pronounced wall thickening towards the basal epicardium. In some regions the mesh is not visible because the deformed geometry has moved in the positive x-direction.

It is worth remarking that fine-mesh simulations for realistic and patient-specific geometries is not possible using only direct solvers due to the excessive memory usage. This issue intensifies in more complex models such as electromechanical tests. Adopting the augmented Lagrangian strategy, even with direct solvers for the top-left block, enables larger-scale and more complex computations.

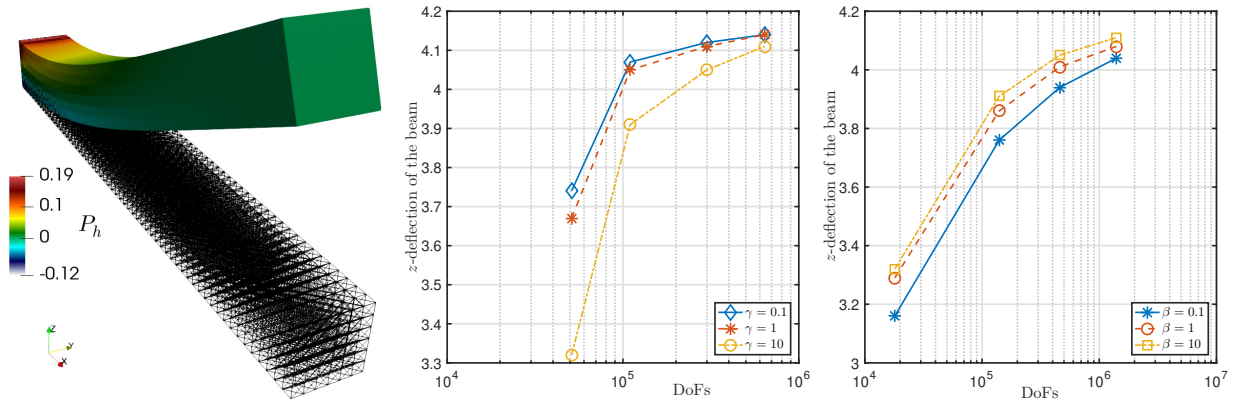

(a) (b) (c)

Figure 5.4: Test 5. (a) deflection of the beam geometry with pressure distribution; (b) plot of deflection magnitudes at $(10, 0.5, 1)$ against the number of degrees of freedom (DoFs) for different values of γ at $\beta = 10$; (c) plot of deflection magnitudes at $(10, 0.5, 1)$ against the number of degrees of freedom (DoFs) for different values of β at $\gamma = 10$.

5.5 Performance of the preconditioner

The accuracy and the performance of the preconditioner are validated through a set of computational benchmark tests introduced in [28]. Detailed descriptions of the problems can be found therein. Here we simulate only the first two tests (namely the beam deflection problem and the ellipsoid inflation problem), since the equivalence of the contraction problem has already been considered in Section 5.4. Quantitative results (i.e. the deflection and inflation magnitudes), which allow us to validate the accuracy of the discretisation and preconditioner are given in the recent work [14], and the performance of the preconditioner can be examined by looking at the average number of outer Krylov iterations per Newton step and total runtime.

The first problem (Test 5) considers a deflecting cuboidal beam whose geometry is defined by $x \in [0, 10]$, $y \in [0, 1]$, $z \in [0, 1]$ mm, with the fibre direction being constant along the x-axis. To match the benchmark test in [28], the transversely isotropic constitutive law is characterised by the strain energy density proposed by Guccione et al. [23]:

$$\Psi_{\mathrm{GCM}} = a/2(e^Q - 1), \tag{5.1}$$

with $Q = b_f E_{ff}^2 + b_t(E_{ss}^2 + E_{nn}^2 + E_{sn}^2 + E_{ns}^2) + b_{fs}(E_{fs}^2 + E_{sf}^2 + E_{fn}^2 + E_{nf}^2)$, where $a = 2\,\mathrm{kPa}$, $b_f = 8$, $b_t = 2$, $b_{fs} = 4$, and the E_{ij} denote entries of the Green–Lagrange strain tensor $\mathbf{E}$, rotated with respect to a local coordinate system aligned with $\boldsymbol{f}_0, \boldsymbol{s}_0, \boldsymbol{n}_0$.

The face $x = 0$ is fixed in all directions and a pressure of 0.004 kPa is applied to the bottom face $z = 0$. The z-coordinate of the end point $(10, 0.5, 1.0)$ after deflection, according to [14], is around 4.15 mm.

The second problem (Test 6) considers the inflation of an ellipsoid-like geometry, simulating the deformation pattern of the left ventricle. As in Test 5, the constitutive relation (5.1) is adopted. The base plane $z = 5$ mm is fixed in all directions, and a pressure of 10 kPa is applied to the endocardial surface. Again by [14], the y-coordinate of the epicardial apex $(0, -23, 0)$ after inflation is around -28.8 mm.

We observe from Figure 5.4 the convergence in deflection magnitudes for different values of penalty parameter γ and pressure stabilisation constant β. The limits agree with the findings in [14], thus validating the accuracy of the discretisation and preconditioner. The performance of the preconditioner at different values of β and γ is illustrated by the following tables.

We observe from Table 5.3 a slight decrease in the number of Krylov iterations as we increase the value of the stabilisation parameter, indicating that our preconditioner is robust to the pressure stabilisation

# refinements	DoFs	stabilisation constant (β)		
		0.1	1	10
1	1.8×10^4	3.55	2.95	2.50
2	1.4×10^5	3.86	2.86	2.45
3	4.6×10^5	3.96	2.86	2.73
4	1.4×10^6	4.29	3.14	2.73

Table 5.3: Test 5. Average number of Krylov iterations per Newton iteration at different values of β, fixing $\gamma = 10$.

# refinements	DoFs	penalty parameter (γ)			
		0.1	1	10	100
1	1.2×10^4	16.0	6.21	2.50	1.36
2	1.4×10^5	17.4	6.60	2.45	NF
3	4.6×10^5	18.0	7.20	2.73	NF
4	1.0×10^6	18.4	7.60	2.73	NF

Table 5.4: Test 5. Average number of Krylov iterations per Newton iteration at different values of γ, fixing $\beta = 10$, where NF denotes the convergence failure of the outer Newton solve. Increasing γ improves the approximation of the Schur complement and reduces the number of outer Krylov iterations, but makes the nonlinear problem more difficult to solve.

	degrees of freedom (DoFs)		
	1.4×10^5	4.6×10^5	1.4×10^6
Direct solver for $\mathcal{A}$	3 min 09 s	24 min 07 s	3 h 12 min 02 s
AL preconditioner with direct solver for A	2 min 25 s	17 min 31 s	1 h 55 min 01 s

Table 5.5: Test 5. Average runtime of solving the problem with LU factorisation (direct solver) applied to the full system, and using the augmented Lagrangian (AL) preconditioner with LU applied to the top-left block A, at $\beta = 10$ and $\gamma = 10$.

employed. On the other hand, Table 5.4 illustrates a large decrease in the number of Krylov iterations as we increase γ. The failure of Newton solve is a direct consequence of the increasing nonlinearity of the problem as γ increases, as the constraint is nonlinear.

Table 5.5 allows us to see how the computational efficiency has improved after adopting the augmented Lagrangian preconditioner. We observe that at each mesh refinement, the average runtime after preconditioning is reduced by roughly 25% (and 40% when DoFs $= 1.4 \times 10^6$) compared to that of solving the test problem using LU factorisation. We expect to see a larger amount of time saved for more complex simulations (i.e. as the number of degrees of freedom increases).

For Test 6, we observe from Figure 5.5 the convergence in inflation magnitudes at the apex for different values of γ and β. Again, the limits agree with the results obtained in [14], thus validating the accuracy of the discretisation and preconditioner.

We observe from Table 5.6 a moderate decrease in the iteration count as we take larger stabilisation parameters, showing that the performance of the preconditioner is robust with respect to the pressure stabilisation employed. As in Test 5, Table 5.7 shows a considerable reduction in the number of Krylov iterations as we take larger values of γ.

Table 5.8 illustrates the average runtime of solving test 6 before and after the adoption of the augmented Lagrangian preconditioner at different mesh refinements. We observe that the computational efficiency of fine simulations is increased by roughly 10–20% compared to that of applying LU factorisation to the whole

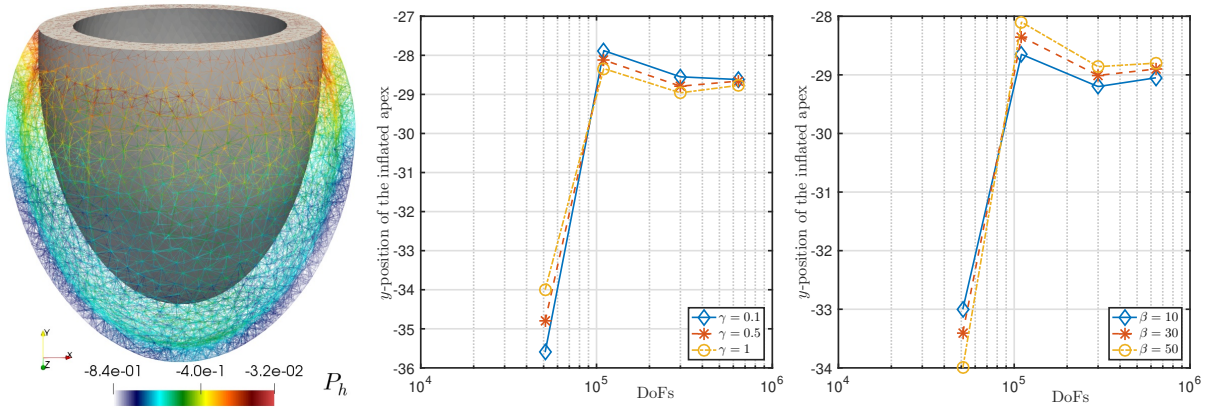

(a) (b) (c)

Figure 5.5: Test 6. (a) inflation of the ellipsoid, pressure is shown by the colour bar; (b) plot of inflation magnitudes at epicardial apex (0,-23,0) against the number of degrees of freedom (DoFs) for different values of γ at $\beta = 50$; (c) plot of inflation magnitudes at epicardial apex (0,-23,0) against the number of degrees of freedom (DoFs) for different values of β at $\gamma = 1$.

# refinements	DoFs	stabilisation constant (β)		
		0.5	5	50
1	5.1×10^4	7.26	5.19	4.18
2	1.1×10^5	7.55	5.38	4.25
3	3.0×10^5	8.65	5.75	4.47
4	6.4×10^5	9.02	6.19	4.57

Table 5.6: Test 6. Average number of Krylov iterations per Newton iteration at different values of β, fixing $\gamma = 1$..

# refinements	DoFs	penalty parameter (γ)		
		0.1	1	10
1	5.1×10^4	14.7	5.19	2.47
2	1.1×10^5	15.4	5.38	2.51
3	3.0×10^5	16.6	5.75	2.58
4	6.4×10^5	17.2	6.19	2.66

Table 5.7: Test 6. Average number of Krylov iterations per Newton iteration at different values of γ, fixing $\beta = 5$.

system. As remarked at the end of Section 5.4, for cardiac electromechanics a much higher mesh resolution is required, and using solely direct solvers for $\mathcal{A}$ is ruled out.

6 Concluding remarks

In this paper we have proposed an extension of a formulation for nonlinear hyperelasticity in the incompressible regime, which uses the Kirchhoff stress as one of the field variables. This formulation presents some advantages related to imposition of stress symmetry, usability in recent models for stress-assisted diffusion, and discretisation using classical conforming spaces. We have discussed the solvability and stability of the

	degrees of freedom (DoFs)		
	1.1×10^5	43.0×10^5	6.4×10^5
Direct solver for $\mathcal{A}$ (serial)	27 min 11 s	2 h 27 min 58 s	11 h 23 min 42 s
AL preconditioner with direct solver for A (serial)	24 min 32 s	2 h 10 min 58 s	9 h 59 min 5 s
Direct solver for $\mathcal{A}$ (8 cores)	6 min 41 s	34 min 16 s	2 h 37 min 0 s
AL preconditioner with direct solver for A (8 cores)	6 min 3 s	30 min 59 s	2 h 20 min 21 s
Direct solver for $\mathcal{A}$ (16 cores)	4 min 24 s	22 min 13 s	1 h 49 min 32 s
AL preconditioner with direct solver for A (16 cores)	4 min 22 s	19 min 51 s	1 h 29 min 59 s

Table 5.8: Test 6. Average runtime of solving the problem with LU factorisation (direct solver) applied to the full system, and using the augmented Lagrangian (AL) preconditioner with LU applied to the top-left block A, at $\beta = 50$ and $\gamma = 10$.

linearised problem, and have proposed an augmented Lagrangian preconditioner. Several numerical examples have demonstrated the performance of the formulation and the robustness of the preconditioner in the solution of some benchmark problems and some tests arising in cardiac biomechanics. Ongoing extensions of this work include the analysis of time-dependent formulations of hyperelasticity and understanding how the preconditioner should be adapted. We also plan to derive suitable a posteriori error estimators. Another important extension is the study of inner iterative solvers for the augmented Kirchhoff stress-displacement block in the preconditioner.

Acknowledgements. The authors are grateful to Xiyao Li (Oxford MMSc programme) for her valuable contributions in the formulation and implementation of the numerical tests and many fruitful discussions. This research has been supported by the Engineering and Physical Sciences Research Council through the grants EP/R029423/1 and EP/V001493/1, by CONICYT-Chile through project Fondecyt 1181748 and project AFB 170001 of the PIA Program: Concurso Apoyo a Centros Científicos y Tecnológicos de Excelencia con Financiamiento Basal; and by the HPC-Europa3 Transnational Access Grant HPC175QA9K.

References

[1] M.S Alnæs, J. Blechta, J. Hake, A. Johansson, B. Kehlet, A. Logg, C. Richardson, J. Ring, M.E. Rognes, and G.N. Wells, *The FEniCS project version 1.5.* Arch. Numer. Softw. (2015), **3(100)**:9–23.

[2] C. Bacuta, *A unified approach for Uzawa algorithms.* SIAM J. Numer. Anal. (2006), **44(6)**:2633–2649.

[3] J. M. Ball, *Convexity conditions and existence theorems in nonlinear elasticity.* Arch. Rational Mech. Anal. (1977), **63**:337–403.

[4] J. M. Ball and F. Murat, *$W^{1,p}$-Quasiconvexity and variational problems for multiple integrals.* J. Funct. Anal. (1984), **58**:225–253.

[5] L. Barbarotta, S. Rossi, L. Dede, and A. Quarteroni, *A transmurally heterogeneous orthotropic activation model for ventricular contraction and its numerical validation.* Int. J. Numer. Methods Biomed. Engrg. (2018), **34(2)**:e3137.

[6] D. Baroli, A. Quarteroni, and R. Ruiz-Baier, *Convergence of a stabilized discontinuous Galerkin method for incompressible nonlinear elasticity.* Adv. Comput. Math. (2013), **39**:425–443.

[7] H.R. Bayat, J. Krämer, L. Wunderlich, S. Wulfinghoff, S. Reese, B. Wohlmuth, and C. Wieners, *Numerical evaluation of discontinuous and nonconforming finite element methods in nonlinear solid mechanics.* Comput. Mech. (2018), **62**:1413–1427.

[8] J.C. Bellido, J. Cueto, and C. Mora-Corral, *Nonlocal hyperelasticity and polyconvexity in fractional spaces.* arXiv preprint (2018), **1812.05848**.

[9] M. Benzi and M. A. Olshanskii, *An augmented Lagrangian-based approach to the Oseen problem.* SIAM J. Sci. Comput. (2006), **28(6)**:2095–2113.

[10] M. Benzi, G.H. Golub, and J. Liesen, *Numerical solution of saddle point problems.* Acta Numerica (2005), **14**:1–137.

[11] M. Benzi and T. Miroslav, *A sparse approximate inverse preconditioner for nonsymmetric linear systems.* SIAM J. Sci. Comput. (1998), **19(3)**:968–994.

[12] D. Boffi, F. Brezzi, and M. Fortin, *Mixed finite element methods and applications.* Springer-Verlag, Heidelberg, 2013.

[13] S.C. Brenner and L.R. Scott, *The Mathematical Theory of Finite Element Methods.* 3rd edn. Texts in Applied Mathematics, vol. 15. Springer, New York, 2008

[14] J.O. Campos, R. Weber dos Santos, J. Sundnes, and B. Martins Rocha, *Preconditioned augmented Lagrangian formulation for nearly incompressible cardiac mechanics.* Int. J. Numer. Methods Biomed. Engrg. (2018), **34(4)**:e2948.

[15] K.S. Chavan, B.P. Lamichhane, and B.I. Wohlmuth, *Locking-free finite element methods for linear and nonlinear elasticity in 2D and 3D.* Comput. Methods Appl. Mech. Engrg. (2007), **196**:4075–4086.

[16] M. Chiumenti, M. Cerevra, and R. Codina, *A mixed three-field FE formulation for stress accurate analysis including the incompressibility limit.* Comput. Methods Appl. Mech. Engrg. (2015), **283**:1095–1116.

[17] P.G. Ciarlet, *Mathematical Elasticity Vol. 1: Three-dimensional Elasticity*, North Holland, Amsterdam, 1988.

[18] H.C. Elman, D.J. Silvester, and A.J. Wathen, *Finite Elements and Fast Iterative Solvers: with applications in incompressible fluid dynamics.* Oxford University Press (2014).

[19] P. E. Farrell, L. Mitchell, and F. Wechsung, *An augmented Lagrangian preconditioner for the 3D stationary incompressible Navier-Stokes equations at high Reynolds number.* SIAM J. Sci. Comput. (2019) **41(5)**:A3073–A3096.

[20] M. Fortin and R. Glowinski, *Augmented Lagrangian methods: applications to the numerical solution of boundary-value problems.* Elsevier (2000), **15**.

[21] G.N. Gatica, *A Simple Introduction to the Mixed Finite Element Method. Theory and Applications*, Springer Briefs in Mathematics, Springer, Cham Heidelberg New York Dordrecht London, 2014.

[22] V. Girault and P.A. Raviart, *Finite Element Methods for Navier–Stokes Equations. Theory and Algorithms.* Springer Series in Computational Mathematics, 5. Springer-Verlag, Berlin, 1986.

[23] J.M. Guccione, K.D. Costa, and A.D. McCulloch, *Finite element stress analysis of left ventricular mechanics in the beating dog heart*, J. Biomech. (1995), **28**:1167–1177.

[24] G.A. Holzapfel and R.W. Ogden, *Constitutive modelling of passive myocardium: a structurally based framework for material characterization.* Phil. Trans. Royal Soc. London A (2009), **367**:3445–3475.

[25] I.C.F. Ipsen, *A note on preconditioning nonsymmetric matrices.* SIAM J. Sci. Comput. (2001), **23**:1050–1051.

[26] H. Kabaria, A.J. Lew, and B. Cockburn, *A hybridizable discontinuous Galerkin formulation for non-linear elasticity.* Comput. Methods Appl. Mech. Engrg. (2015), **283**:303–329.

[27] B.P. Lamichhane and E.P. Stephan, *A symmetric mixed finite element method for nearly incompressible elasticity based on biorthogonal systems*. Numer. Methods PDEs (2012), **28(4)**:1336–1353.

[28] S. Land, et al., *Verification of cardiac mechanics software: benchmark problems and solutions for testing active and passive material behaviour*, Proc. R. Soc. A. (2015), **471(2184)**:20150641.

[29] P. Le Tallec, *Existence and approximation results for nonlinear mixed problems: Application to incompressible finite elasticity*. Numer. Math. (1982), **38**:365–382.

[30] C. Mardare, *A nonlinear Korn inequality with boundary conditions and its relation to the existence of minimizers in nonlinear elasticity*. C. R. Math. (2011), **349(3–4)**:229–232.

[31] B. Müller, G. Starke, A. Schwarz, and J. Schröder, *A first-order system least squares method for hyperelasticity*. SIAM J. Sci. Comput. (2014), **36(5)**:B795–B816.

[32] M.F. Murphy, G.H. Golub, and A.J. Wathen, *A note on preconditioning for indefinite linear systems*. SIAM J. Sci. Comput. (2000), **21**:1969–1972.

[33] A. Propp, A. Gizzi, F. Levrero-Florencio, and R. Ruiz-Baier, *An orthotropic electro-viscoelastic model for the heart with stress-assisted diffusion*. Biomech. Model. Mechanobiol. (2020), **19(2)**:633–659.

[34] F. Rathgeber, D.A. Ham, L. Mitchell, M. Lange, F. Luporini, A.T.T. McRae, G.-T. Bercea, G.R. Markall, and P.H.J. Kelly, *Firedrake: automating the finite element method by composing abstractions*. ACM Transact. Math. Softw. (2017), **43(3)**:24.

[35] S. Rossi, T. Lassila, R. Ruiz-Baier, A. Sequeira, and A. Quarteroni, *Thermodynamically consistent orthotropic activation model capturing ventricular systolic wall thickening in cardiac electromechanics*. Eur. J. Mech. A/Solids (2014), **48**:129–142.

[36] R. Ruiz-Baier, A. Gizzi, A. Loppini, C. Cherubini, and S. Filippi, *Thermo-electric effects in an anisotropic active-strain electromechanical model*. Comm. Comput. Phys. (2020), **27(1)**:87–115.

[37] Y. Saad, *A flexible inner-outer preconditioned GMRES algorithm*. SIAM J. Sci. Comput. (1992), **14**:461–469.

[38] A. Schwarz, K. Steeger, M. Igelbüscher, and J. Schröder, *Different approaches for mixed LSFEMs in hyperelasticity: Application of logarithmic deformation measures*. Int. J. Numer. Methods Engrg. (2018) **115(9)**:1138–1153.

[39] E. Stein and M. Rüter, *Finite Element Methods for Elasticity with Error-controlled Discretization and Model Adaptivity*, in Encyclopedia of Computational Mechanics, E. Stein, R. de Borst, and T. Hughes, eds., Wiley, 2004, pp. 5–58.

[40] T. Valent, *Boundary Value Problems of Finite Elasticity: Local Theorems on Existence, Uniqueness, and Analytic Dependence on Data*. Springer-Verlag, 1988.

[41] A.J. Wathen, *Preconditioning*. Acta Numerica (2015), **24**: 329–376.

[42] J. Whiteley, *A preconditioner for the finite element computation of incompressible nonlinear elastic deformations*, Comput. Mech. (2017), **60**:683–692.

[43] P. Wriggers, *Nonlinear Finite Element Methods*. Springer-Verlag, Berlin, 2008.

[44] K. Zhang, *Energy minimizers in nonlinear elastostatics and the implicit function theorem*. Arch. Rational Mech. Anal. (1991), **114**:95–117.

Centro de Investigación en Ingeniería Matemática (CI^{2}MA)

PRE-PUBLICACIONES 2020

2020-06 Tomás Barrios, Rommel Bustinza, Camila Campos: *A note on a posteriori error estimates for dual mixed methods*

2020-07 Raimund Bürger, Elvis Gavilán, Daniel Inzunza, Pep Mulet, Luis M. Villada: *Numerical simulation of forest fires by IMEX methods*

2020-08 Rommel Bustinza, Jonathan Munguia: *An a priori error analysis for a class of nonlinear elliptic problems applying the hybrid high-order method*

2020-09 Ngoc-Cuong Nguyen, Jaime Peraire, Manuel Solano, Sébastien Terrana: *An HDG method for non-matching meshes*

2020-10 Rommel Bustinza, Jonathan Munguia: *A mixed Hybrid High-Order formulation for linear interior transmission elliptic problems*

2020-11 Gabriel N. Gatica, Antonio Marquez, Salim Meddahi: *A mixed finite element method with reduced symmetry for the standard model in linear viscoelasticity*

2020-12 Raimund Bürger, Gerardo Chowell, Leidy Y. Lara-Diaz: *Measuring the distance between epidemic growth models*

2020-13 Jessika Camaño, Carlos Garcia, Ricardo Oyarzúa: *Analysis of a new mixed-FEM for stationary incompressible magneto-hydrodynamics*

2020-14 Raimund Bürger, Paola Goatin, Daniel Inzunza, Luis M. Villada: *A nonlocal pedestrian flow model accounting for anisotropic interactions and walking domain boundaries*

2020-15 Felipe Lepe, David Mora, Gonzalo Rivera, Iván Velásquez: *A virtual element method for the Steklov eigenvalue problem allowing small edges*

2020-16 José Querales, Rodolfo Rodríguez, Pablo Venegas: *Numerical approximation of the displacement formulation of the axisymmetric acoustic vibration problem*

2020-17 Patrick E. Farrell, Luis F. Gatica, Bishnu Lamichhane, Ricardo Oyarzúa, Ricardo Ruiz-Baier: *Mixed Kirchhoff stress - displacement - pressure formulations for incompressible hyperelasticity*

Para obtener copias de las Pre-Publicaciones, escribir o llamar a: Director, Centro de Investigación en Ingeniería Matemática, Universidad de Concepción, Casilla 160-C, Concepción, Chile, Tel.: 41-2661324, o bien, visitar la página web del centro: http://www.ci2ma.udec.cl







Centro de Investigación en
Ingeniería Matemática (CI²MA)
Universidad de Concepción

Casilla 160-C, Concepción, Chile
Tel.: 56-41-2661324/2661554/2661316
http://www.ci2ma.udec.cl